

Chapter 4

Analysis of Polarization Maps

4.1 The $H\alpha$ Images and Polarization Maps

In order to present the polarization in an understandable form, maps of the polarization across the nebulae were made. The polarization images of the Rosette Nebula will be discussed in full detail. Other regions in Cygnus will be presented, however, a full discussion of the reduction steps for these images would only be a redundant discussion of the same steps used to reduce the Rosette Nebula insofar as the nominal reduction steps are concerned and the steps used to produce the actual polarization map.

The nominal reduction steps were presented in chapter 2, section 2.4.1 and were shown to be necessary to remove any camera signature from the images. These signatures include the bias level and pixel-to-pixel variations of the CCD. To remove these, a bias image was subtracted from all of the images and each image was divided by a flat-field image. All images were then transposed so that the first pixel corresponded to the lower left-hand corner instead of the upper left-hand corner. Finally, each image was sliced down to two dimensions.

Since these images form the Stoke's parameters I , Q , and U which are formed by sums and differences between images, any cosmic ray hits will mimic signals that are not truly present. Therefore, signals produced by cosmic rays needed to be removed before the alignment and creation of the Stoke's parameter

images. To do this the task `COSMICRAYS` in the `CCDRED` package of `IRAF` was run on each of the images. This works by locating "brightest" pixel in a 5×5 detection window. The mean in the detection window is computed without the two highest pixel values, and if the highest pixel value is 25 times greater than this mean, then the pixels in the box are replaced by the average of the four neighboring pixels. Real objects such a nebulae, which have a large dimension compared to the sizes of stars are not strongly affected by this routing and so remain unchanged.

At this point the images are aligned using the task `IMALIGN` which was discussed in section 2.4.3 of chapter 2. There it was shown that using the bicubic spline as the shifting parameter does not significantly alter the data. Seventy nine bright stars were chosen in the first image as reference stars. Accurate centers for these stars were computed using the task `CENTER` in the `APPHOT` package of `IRAF` and all subsequent images were aligned to these references. A check of the alignment was done by visually blinking the images to try to notice any large scale shifting of the images. Since no large shifts were visible, a few stars were selected and their positions measured before and after shifting. A check of the standard deviation indicated that the error in the shifting was reduced by a factor of ~ 5 and was ≤ 0.1 pixels. Since each pixel is $1'.6$ (or $96''$) this correspond to error on the order of ten arcsecond which is much less than one pixel.

The next step was to create the Stoke's parameter images Q and U (as well as the normalized Stoke's parameter images q and u) by differences between images recorded with the polarizer at different position angles. Since the polarizer was positioned at every 45° from 0° to 315° , the creation of the Stoke's parameter images I , Q , and U were obtained by

$$I = I(0^\circ) + I(90^\circ) = I(180^\circ) + I(270^\circ) \quad (4.1)$$

$$Q = I(0^\circ) - I(90^\circ) = I(180^\circ) - I(270^\circ) \quad (4.2)$$

$$U = I(45^\circ) - I(135^\circ) = I(225^\circ) - I(315^\circ) \quad (4.3)$$

as was discussed in previous chapters. Once I , Q , and U images were made, the removal of a background was necessary. This was necessary since the Stoke's parameter image I contains a background from each of the two images

added to create this one, resulting in a background for I that is approximately twice the background of any one of the individual images. It was necessary to remove a background from the Q and U images as well since any polarized background would not subtract out.

The images were examined by plotting lines and columns in some of the images to see at least qualitatively what the background looked like. Particularly, plots were made in regions where there were no bright HII regions. All plots showed no noticeable gradient and so each images was considered to be the sum of a signal plus a background (i.e., $I = I_s + I_b$, $Q = Q_s + Q_b$, and $U = U_s + U_b$). A constant background was determined for each of the Stoke's parameter images by determining the median value in box which spanned the image and circumscribed a 10° diameter circle centered on the image. This value was then subtracted from each of the three Stoke's parameter images. (A sample of a plotted row before and after subtraction is shown in Figure 4.1.) From these background subtracted images the normalized Stoke's parameter images were obtained by $q = Q_s/I_s$ and $u = U_s/I_s$. Individual maps of q and u were made by the above procedure and an average total intensity image was made by averaging all of the separate total intensity images using the `IMCOMBINE` task in `IRAF`. The appropriate parameters were set so that the images were averaged on a pixel-by-pixel basis without any pixel rejection.

The next step was to remove most of the very bright stars from the images of I , q and u since they are of no concern in the polarization maps of the extended HII regions. Also, these stars tended to leave residuals in the images which produced large polarizations in the maps. However, before their removal, eleven bright stars were used to first determine the coordinate system parameters for the total intensity image. Since the q and u images are aligned with the total intensity image, it was only necessary to find the parameters for this image. The discussion of these parameters and the tagging of the image header was discussed in chapter 2, section 2.4.2. and so will not be discussed here.

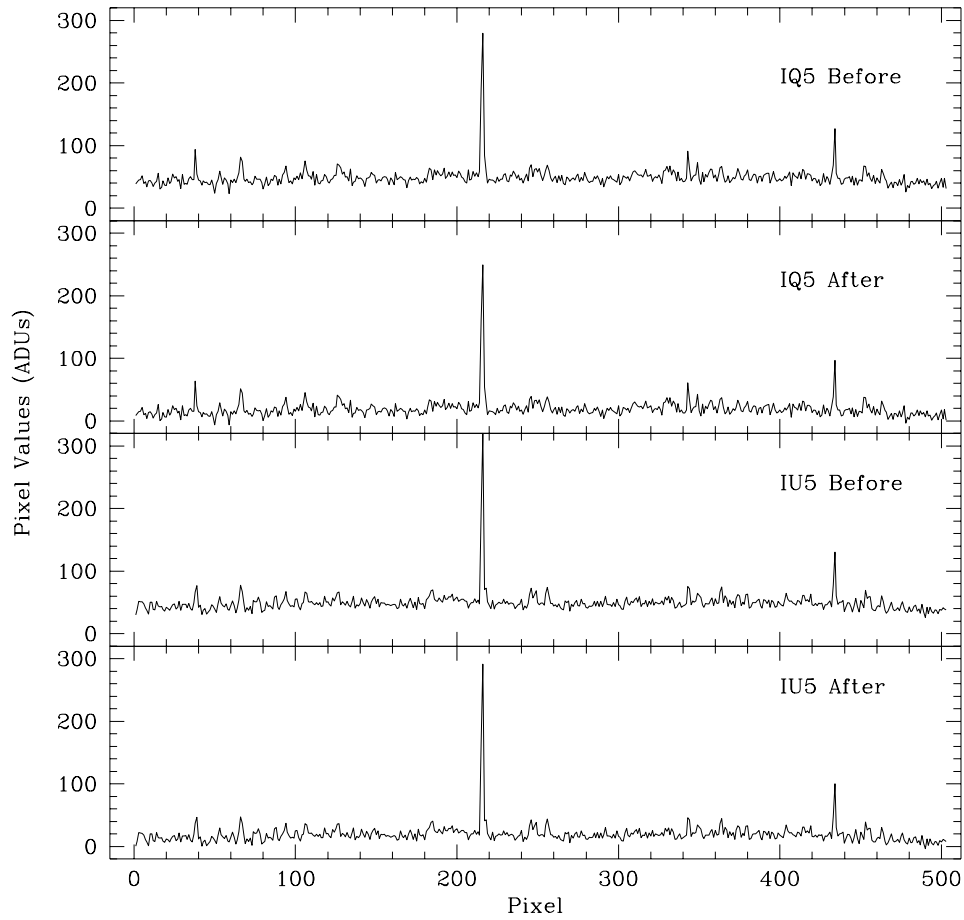


Figure 4.1 Line plots through regions of the total intensity images where no bright $H\alpha$ structures were present.

First, the bright stars were located using the `DAOFIND` task in the `APPHOT` package. The `DAOFIND` task was run on each image with a threshold set to detect any stars greater than fifteen times the background standard deviation. For each image the number of stars detected was noted and a list of their positions recorded for the one image that had the maximum number of stars detected. While the number of stars should remain the same in each image, it was nonetheless discovered that some of the not so bright stars were not detected in some of the images.

This list was then used as the input of stellar positions in the task `IMEDIT` which was used to remove these bright stars. This task removed these stars by replacing all the pixels in a 5×5 box centered on each star with zeros. This was chosen over the choice of filling the box with pixels that were a mean of the surrounding background with gaussian noise added so that no false or extraneous data would be introduced into the images. The total intensity image, however, had to be handled in a slightly different manner.

Since a contour map of the Rosette Nebula was desired, a quick contour map was made using the total intensity image with the stars removed. However, it was seen on the map that box-like contours surrounded the locations of removed stars. In order to remedy this, a second total intensity image was made using the method described above but with 25 pixels replaced by the mean of the surrounding background with gaussian noise added. Since this image would only serve as the contour image, no loss of data or introduction of significantly false data had any great effect on the contouring process.

Finally, a set of q , u , and average total intensity images were copied to another subdirectory and smoothed in order to increase the signal-to-noise ratio. The smoothing was accomplished by means of the task `BOXCAR` in `IRAF` which averaged all of the pixels in a 3×3 grid and replaced the center pixel by this average value. This was done for every pixel in the image except near the edges where a constant value was used. (Since pixels near the edge are not useful, this was not a problem.)

The actual polarization maps were created by two programs and the Super Mongo[®] plotting software. The first program, `mapstat.f`, read in the q , u , and total intensity images and computed the mean, variance, standard deviation, and standard deviation of the mean on a pixel-by-pixel basis for both the q and u

images. Anywhere the total intensity was zero, (indicating a replacement for a bright star), all statistical quantities were set to zero. For each of these statistical quantities, FITS images were written. A second program, `mapmaker.f`, then read in the average q and u images, as well as their variance images, and computed the percent polarization and position angle. Any position which had a zero in the statistical maps had a zero for the percent polarization and position angle as well. (Both programs used above are listed in the appendix.)

Using the same procedure above, another program similar to `mapstat.f` called `mapstatm.f` which uses the trimmed mean instead of the regular mean to compute the average q and u images was created. The statistics were also created for these images as well. This includes calculation of the Winsorized variance, standard deviation, and standard deviation of the mean. The statistics were also created using the methods discussed in section 3.4.4 of chapter 3. Finally, FITS images were made of all of these images.

In order to create a graphical representation of the polarization data, a small program was written which created the appropriate plotting command for Super Mongo[®] to read. This program reads in two lists of pixel positions and values for percent polarization and position angle which were created using the LISTPIX task in IRAF, and computes the necessary beginning and ending points for each of the polarization vectors. This program then writes this information out to a file with appropriate commands which Super Mongo[®] can interpret. The program also requires input information on the lowest value of intensity to plot a vector for, as well as any magnification factor the user desires to apply to the polarization vectors. The lowest intensity value is used so that polarization vectors which are below a certain value are not plotted. Therefore, a contouring of the nebula which is performed by Super Mongo[®] with the lowest contour set at three times the standard deviation above background will result in an image with polarization vectors only inside this lowest contour.

For the large images, a mask was applied so that vector outside the inner 10° were not plotted. The reason these pixels were not useful was discussed in chapter 2, section 2.2.3. For smaller regions of interest, the same method for making the plot was also used, however, only a list of pixels in the regions of interest were made using the LISTPIX task in IRAF.

4.2 Calibration of H α Total Intensity Map

In order to make comparisons with other published data, the total intensity map I of the Rosette Nebula needed to be calibrated in appropriate units of intensity. Since the units of intensity in the MKS system are Joules $\text{s}^{-1}\text{m}^{-2}\text{sr}^{-1}$ and each pixel only records analog digital units (ADU, or simply "counts"), a calibration method was needed to convert the recorded counts into the proper units of intensity. The intensity will also be expressed in Rayleighs, where 1 Rayleigh = $10^6/4\pi$ photons $\text{cm}^{-2}\text{s}^{-1}\text{sr}^{-1} = 2.4 \times 10^{-10}$ W $\text{m}^{-2}\text{sr}^{-1}$ at the H α wavelength.

Fortunately, a calibrated H α photoelectric map of the Rosette Nebula was made by Celnik (1983). This map covers an area of approximately 6.25 square degrees centered on the Rosette Nebula and was made using a photoelectric photometer and narrow bandpass interference filter which isolated the H α line. The resulting intensity map was integrated in concentric rings around the central minimum at $6^{\text{h}} 29^{\text{m}} 01.^{\text{s}}7$, $+ 5^{\circ} 00' 53''$ (1950.0) which resulted in a total H α flux density of $(4.91 \pm 0.34) \times 10^{-11}$ W m^{-2} in a circular radius of $60'$.

This flux density measurement by Celnik (1983) allows us to calibrate our total intensity H α image in the following manner. Since we wish to convert from counts to units of intensity in W $\text{m}^{-2}\text{sr}^{-1}$, we need some calibration constant K such that

$$I(\Omega) = K C(\Omega) \quad (4.4)$$

where $I(\Omega)$ is the specific intensity in W $\text{m}^{-2}\text{sr}^{-1}$ for a solid angle subtended by one pixel in the total intensity image and $C(\Omega)$ is the number of counts in that pixel. Therefore, the calibration constant must have units of W $\text{m}^{-2}\text{sr}^{-1}\text{count}^{-1}$.

Now the flux density is simply the integration of the specific intensity over a certain subtended solid angle. In this particular instance we know the flux density over the solid angle subtended by the circle of $60'$ radius. So using equation (4.4) we may write

$$F = \int I(\Omega) d\Omega = \int K C(\Omega) d\Omega \quad (4.5)$$

where F equals $4.91 \times 10^{-11} \text{ W m}^{-2}$ and the integration is carried out over the $60'$ radius circle centered on the Rosette Nebula. Therefore, by integrating the number of counts in the $60'$ circle we can obtain the calibration constant by simple division.

We can obtain, with reasonable accuracy, the number of counts in an aperture of $60'$ radius centered on the central minimum above by using the PHOT task in the APPHOT package of IRAF. This photometry task uses partial pixels which approximates the region with an irregular polygon, Davis (1987). For this purpose, a circular $60'$ aperture was centered on the central minimum. The off-aperture was a concentric annulus whose inner radius was $80'$ and had a width of $48'$ to allow a large sampling of background pixels. The highest 5% of background pixels were rejected and a gaussian reiteratively fitted by non-linear least squares to the remaining pixel distribution after rejecting any strongly deviant pixels (i.e. pixels greater or less than 3σ). The resulting off value is the background per pixel. This off value was scaled to the area of the on-aperture by multiplying the off value by the area of the on-aperture in pixels. This scaled off value was then subtracted from the number of counts in the on-aperture. The above procedure resulted in a background subtracted flux density of 673,670 counts in an irregular polygonal aperture of $60'$ radius containing 4420 pixels. Since the integration time of the total intensity image was 30 seconds, the number of counts per second is 22,420.

Since the method employed above uses the finite solid angle of a pixel, we can not use equation (4.5) in its present form, but rather we must convert the integral into a summation over the number of pixels in the on aperture

$$F = K \int C(\Omega) d\Omega = K \sum_{i,j} C_{i,j}(\Omega) \Delta\Omega_{pix} \quad (4.6)$$

where $\Delta\Omega_{pix}$ is the solid angle of one pixel which equals $2.1\bar{6} \times 10^{-7} \text{ sr}$. Since this value is the same for each pixel, it comes out of the summation leaving only the total sum of counts in the aperture. Therefore, the calibration constant is found by dividing the known flux density by area of a pixel in steradians and the total number of counts per second in the aperture

$$K = \frac{F}{\Delta\Omega_{pix} \sum_{i,j} C_{i,j}(\Omega)} \quad (4.7)$$

which yields $K = 1.01 \times 10^{-8} \text{ W m}^{-2} \text{ sr}^{-1} \text{ count}^{-1}$. By knowing K we are now able to convert the number of counts in a pixel to the M.K.S units of intensity.

In order to check the accuracy of our procedure, the mean radial distribution of $\text{H}\alpha$ in the total intensity image was obtained in a manner similar to that of Celnik (1983). Celnik's figure 3 is a radial distribution of $\text{H}\alpha$ integrated in rings of $2'$ width about the central minimum. While the horizontal scale in his graph is in arcminutes, the vertical scale is in units of 10^{12} i.f.u. (intensity flux units) per beam, where $1 \text{ i.f.u. per beam} = 6.67 \times 10^{-21} \text{ W m}^{-2} \text{ sr}^{-1}$. Accordingly, photometry was performed on the Rosette Nebula by successive apertures of $2'$ size difference. The background was determined in the manner described above, and the difference in successive apertures was divided by the difference in area. This resulted in a mean radial profile for the total intensity image. For comparison with Celnik's result, we scaled our measurements by first converting counts to intensity and then intensity into units of 10^{12} i.f.u. per beam. The result is shown in Figure 4.2 below along with a plot of Celnik's radial distribution which was obtained by reading off and plotting numbers from his graph.

It is clear from Figure 4.2 that the two curves agree very well with the exception of the inner $10'$. Whereas Celnik (1983) has removed the stars in and around the nebula by fitting and removing a gaussian, we have not done so for stars in the Rosette Nebula in the total intensity image. As a result, the central cluster of stars is likely a cause of the apparent increased emission seen in the central region in Figure 4.2.

We are confident in the calibration constant obtained in this section. This constant allows us to convert our measurements of counts into a more meaningful measurement of intensity, particularly for comparison with published results.

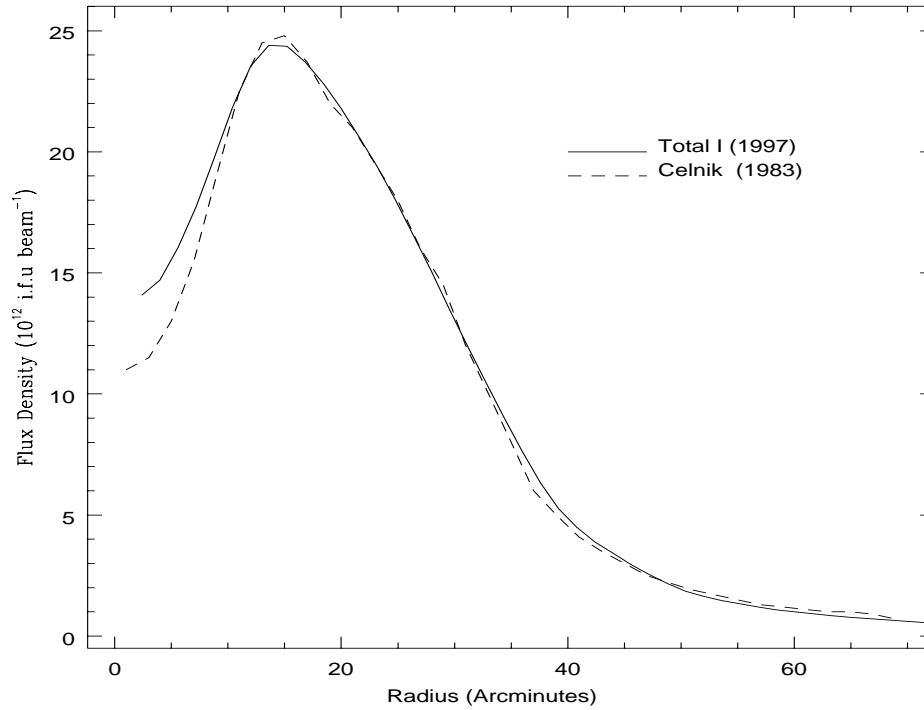


Figure 4.2 Mean radial distribution of H α emission in the total intensity image (solid line) compared with that obtained by Celnik (1983) (dashed line) as a function of distance in arcminutes from the central minimum of the Rosette Nebula. 1 i.f.u. per beam = $6.67 \times 10^{-11} \text{ W m}^{-2} \text{ sr}^{-1}$.

4.3 Overview of the Monoceros Region

As seen in Figure 4.3, this portion of the Monoceros constellation has three objects which are bright in $H\alpha$. Most noticeable are the HII regions in the north and the Rosette Nebula in the southwest. The Monoceros supernova remnant is visible at the center of the image. All of these are labeled on Figure 4.3. Also noticeable to the south is the smaller HII region Sharpless 280 (S280) which is within the usable 10° diameter of the image. As much as there is in this image, there are still a lot of other objects which are present but are not recognizable from this image. Table 4.1 is a list of some of the objects (including those listed above) which are in this region. Figure 4.4 is a labeled contour image of this region.

Table 4.1
PARTIAL LIST OBJECTS IN THE MONOCEROS REGION IN FIGURE 4.3
(1950.0)

Object	Right Ascension	Declination	Type	Comments
Monoceros SNR	06 ^h 37 ^m	+06° 43'	SNR*	Center Coordinates
NGC 2264	06 38	+09 57	Em [†]	Cone Nebula
NGC 2237	06 30	+05 00	Em	Rosette Nebula
S280	06 32	+02 40	Em	Sharpless 280
NGC 2236	06 27	+06 52	Oc ^{††}	
NGC 2244	06 30	+04 54	Oc	In Rosette Nebula
Trumpler 5	06 34	+09 29	Oc	
NGC 2252	06 32	+05 25	Oc	
NGC 2254	06 33	+07 43	Oc	
NGC 2259	06 36	+10 56	Oc	
NGC 2264	06 38	+09 56	Oc	S Mon

*Supernova Remnant

[†]Emission Nebula (HII Region)

^{††}Open Cluster

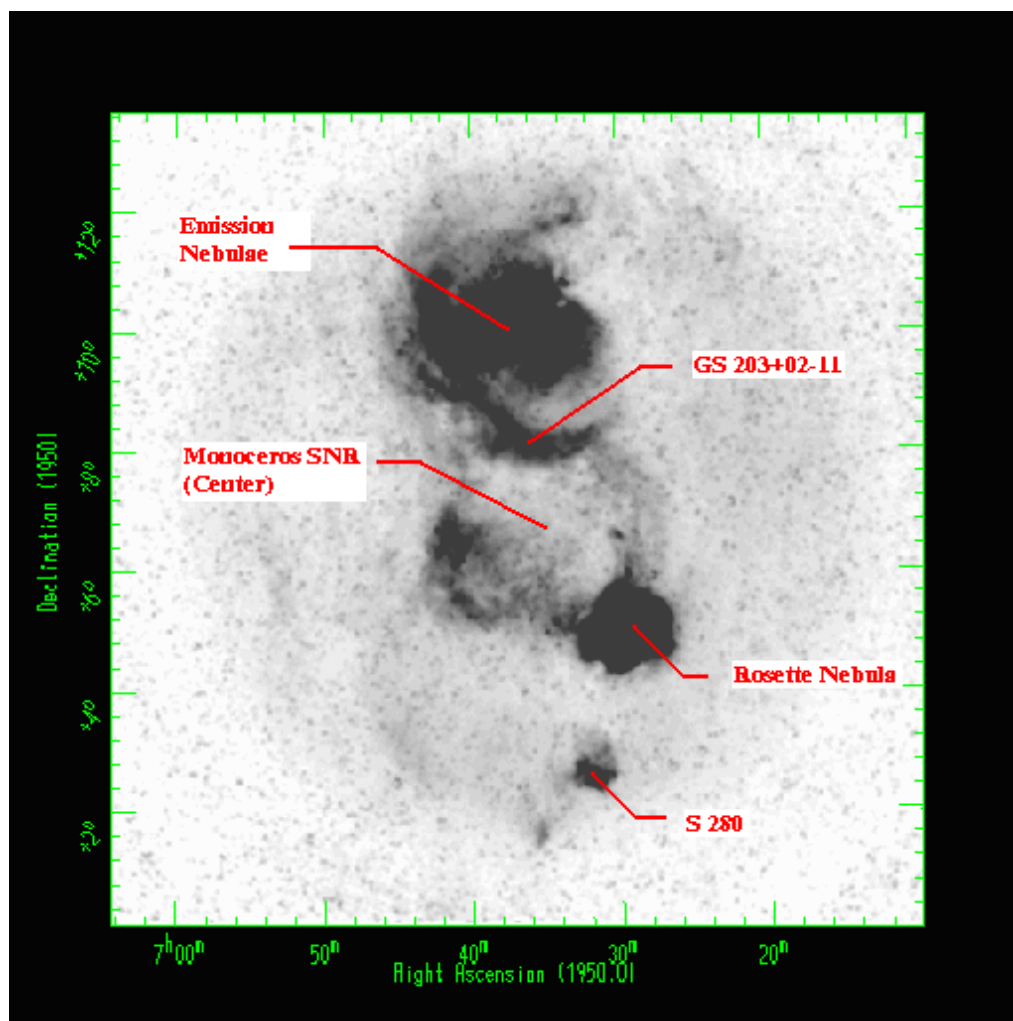


Figure 4.3 Total intensity H α image of the northern Monoceros region with select nebulae marked.

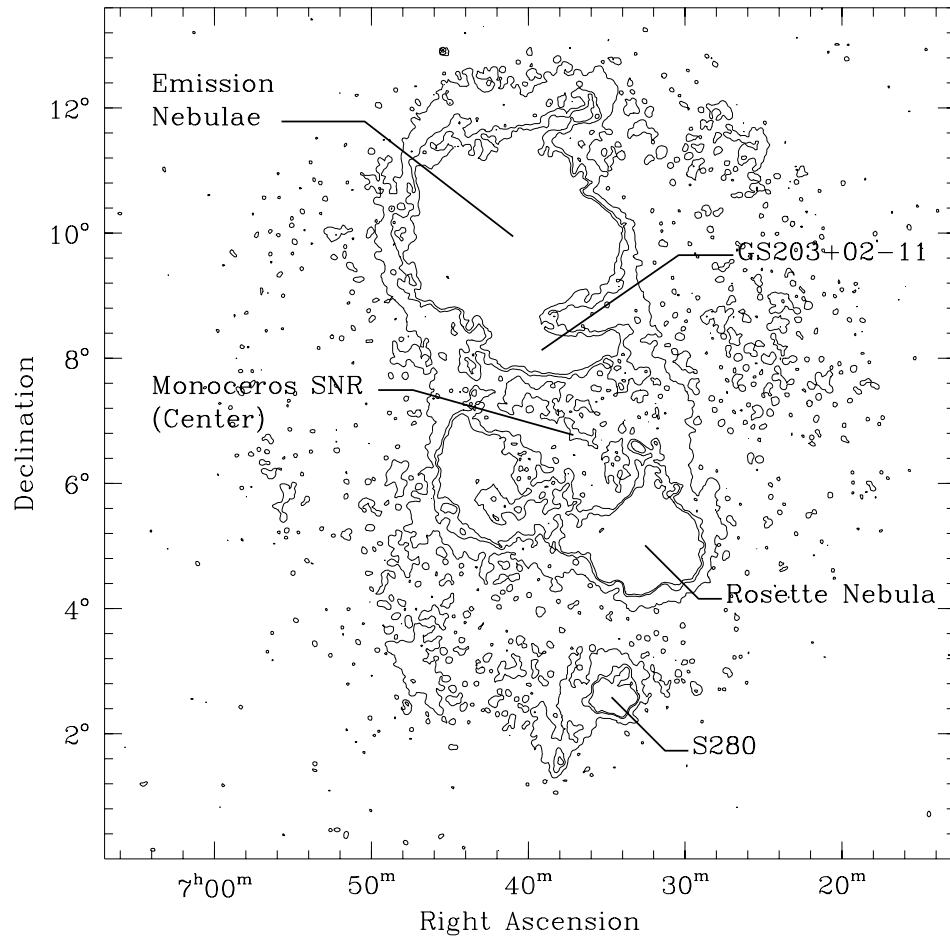


Figure 4.4 Contour plot of total intensity H α image of Figure 4.3 with select nebulae marked.

Sharpless 280

The small nebulosity located to the south east of the Rosette Nebula is Sharpless 280 (S280), an HII region first cataloged by Sharpless (1959) and first identified as a radio source by Davies (1963). Very little information exists about this particular HII region, however radio observations were made by Holden (1968), Haslam and Salter (1971), and Felli and Churchwell (1972). Using these observations, Goudis (1976) has shown that the integrated flux density spectrum over S280 shows a typical thermal shape over frequency range of ~ 100 to 1000 MHz. The flat spectral index indicates that S280 is indeed an optically thin HII region

Located at right ascension $6^{\text{h}} 32^{\text{m}}$ declination $+2^{\circ} 40'$ (1950.0), S280 has an angular extent of about $20'$. At a distance of 1.9 kpc, this translates into a linear extent of about 32 pc. The object is located farther way than the Rosette Nebula, which is at a distance of 1.6 kpc, and its velocity with respect to the local standard of rest is listed by Lang (1991) as $+14.4$ km s $^{-1}$. In the H α image this nebula appears quite bright with an integrated H α flux density of $\sim 4 \times 10^{-4}$ W m $^{-2}$ sr $^{-1}$. No other analysis was done on this object, and it is evidently not a wind blow shell or supershell.

The Emission Nebulae

Located north of the Monoceros supernova remnant is a region of H α nebulosity. Within this region are several small emission nebulae as well as open star clusters and the Monoceros OB1 association. The emission nebulae include NGC 2245 ($6^{\text{h}} 30^{\text{m}}$, $+10^{\circ} 12'$), NGC 2247 ($6^{\text{h}} 30^{\text{m}}$, $+10^{\circ} 23'$), NGC 2261 ($6^{\text{h}} 36^{\text{m}}$, $+8^{\circ} 46'$), and NGC 2264 (Sharpless 273) at $6^{\text{h}} 38^{\text{m}}$, $+9^{\circ} 57'$. (All coordinates are 1950.0 epoch.) Most of these HII regions are rather small in angular size though ($\sim 2' - 10'$) and the most likely cause of H α emission is from the Monoceros OB1 association. In addition to these emission nebulae, there are the dark nebulae Lynds 1264 and 1605. Various star clusters are in this region as well, namely NGC 2251, 2259, and VDB 76, 77, 78. The total extent of this region is approximately 2° circular and appears quite bright in H α . Since none of these nebulae, or star clusters, were the focus of this research, we shall not discuss them any further. However, there is an "arch" of nebulosity to the south of this region that was targeted for study.

GS203+02-11

The curved nebulosity just below the emission nebulae and situated at the northern point of the Monoceros supernova remnant suggest that it may be part of a larger shell structure, possibly GS203+02-11 which was mapped by the Maryland-Greenbank 21 cm sky survey (Westerhout and Wendlandt 1982). This shell, GS203+02-11, is discussed by Oliver et al. (1996) in their CO survey of the Monoceros OB1 region. The center is located at $6^{\text{h}} 35^{\text{m}}, 9^{\circ} 34'$ (1950.0) and is approximately $4^{\circ} \times 5^{\circ}$ as measured HI emission. From a study of the HI velocity distribution of the shell and CO ($J = 1 \rightarrow 0$) line at 115 GHz, as well as energetics, Oliver et al. (1996) find that the shell might be coupled to the bright, curved HII nebulosity labeled GS203+02-11 in Figure 4.3 and 4.12. We shall assume that the curved $H\alpha$ emission seen in Figure 4.3 is associated with the shell GS203+02-11.

Due to its curved nature, this filament was targeted for study by this project. However, as can be seen in the polarization image of this region Figure 4.5 no significant polarization was seen associated with this object. Any polarization vectors that are seen is most likely due to the following: 1) an incomplete subtraction of the background polarization, 2) faint stars remaining in the image, or 3) residual polarization from stars which were removed from the image. Most of the vectors are undoubtedly the residue left from an incomplete subtraction of a polarized background since there is very little correlation between faint stars and the patches of polarization and the residual from removed stars.

A possible reason for the non-detection of the polarization may due to the following. If the density of dust is low, polarization by selective extinction may not be detectable. The grains may not be aligned with the magnetic field. If the temperature and/or density of the gas is sufficiently high, then random collisions of the gas with dust grains may tend to randomize the orientation of the grains. It may be just as likely that the polarization is too low to detect. Typical values of polarization by selective extinction are usually on the order of a few percent or less. As seen with the study of polarization by selective extinction of starlight, values this low are possible, however, the circumstances of measurement for stellar polarization are different from that used to make the large maps in this section.

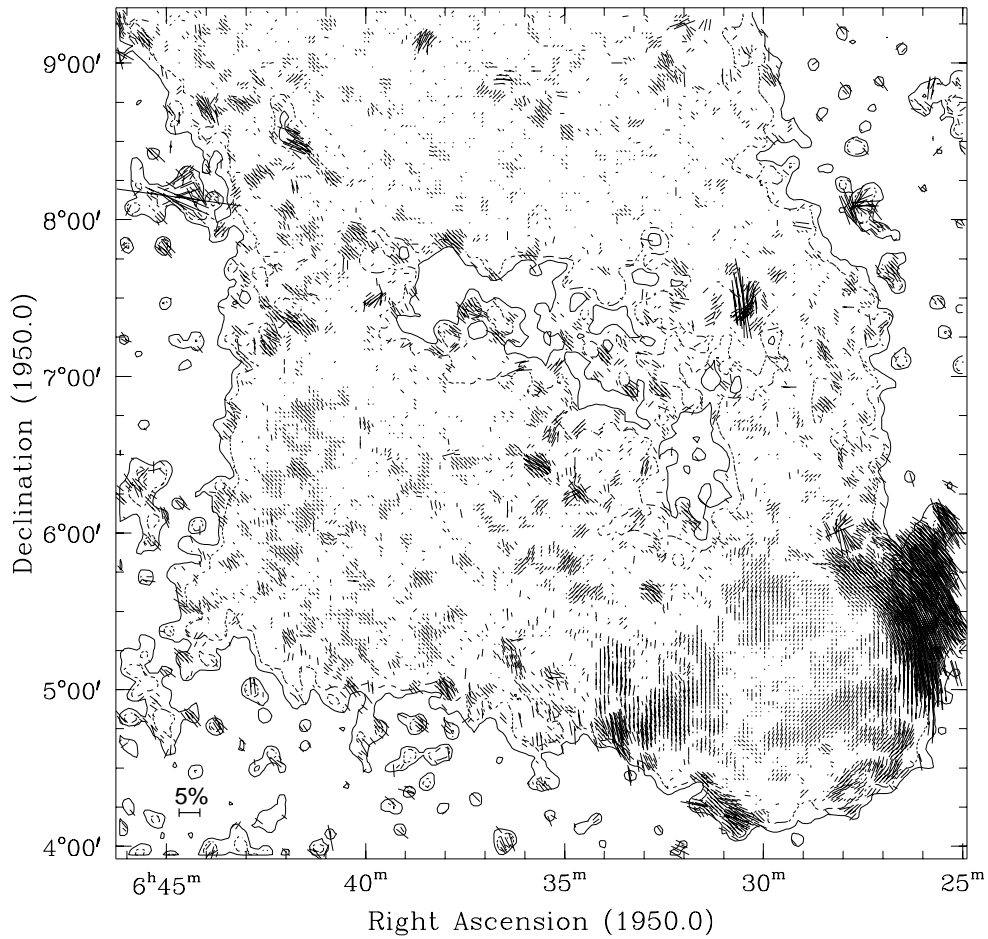


Figure 4.5 Polarization vectors plotted over a contour map of the total intensity image of the Monoceros supernova remnant (*center*), the Rosette Nebula (*lower right corner*), and the northern filament ($45^{\text{m}} < \alpha < 30^{\text{m}}$, $9^{\circ} 0' < \delta < 7^{\circ} 30'$). Contours are 3σ (*solid*) and 5σ (*dashed*) above background.

The Monoceros Supernova Remnant

The Monoceros supernova remnant is the ring-like object located centrally in Figure 4.3 and 4.14. First recognized as a possible supernova remnant by Davies (1963), this region has been explored in both the radio and optical wavelengths as well as X-ray. Leahy et al. (1985, 1986) were the first to detect X-ray emission from the remnant, thus revealing its supernova nature. $H\alpha + [N II]$ images by Davies (1978) and Kirschner et al. (1978) show filamentary structures as well as diffuse emission across the extent of the remnant. Our $H\alpha$ image, Figure 4.6, also reveals the diffuse nature of HII emission across the remnant. Radio observations by Day et al. (1972) and Graham et al. (1982) have shown that a correlation exist between the bright radio emission and the optical filaments.

The distance to the supernova remnant has been a matter of much debate. Estimates have ranged from around 800 pc to about 1.6 kpc. However, Odegard (1986) has reviewed the available evidence from various researchers and argues quite convincingly that the Monoceros supernova remnant is most likely at the same distance as the Monoceros OB2 association. Odegard's (1986) decameter observations seem to indicate that nonthermal emission from the supernova remnant is being absorbed by the Rosette Nebula, placing a further constraint on the distance and suggesting that at least this portion of the remnant is behind the Rosette Nebula. The ~ 1.5 kpc distance to the Monoceros supernova remnant is also supported by Leahy's (1985, 1986) X-ray observations. They find that observations are *best* fit to a supernova model whose distance is 1.5 kpc and whose age is on the order of 3×10^4 years. Since models and observations from other researchers suggests a distance of about 1.5 kpc, we shall adopt this as the distance to the center of the remnant.

From Figure 4.6 it's seen that the Monoceros supernova remnant is approximately circular with a diameter of about $\sim 3.5^\circ$. At a distance of 1.5 kpc, this implies an approximate linear diameter of 100 pc. The surface brightness of the remnant is very low, typically on the order of a few tens of Rayleighs (1 Rayleigh = $10^6/4\pi$ photons $\text{cm}^{-2}\text{s}^{-1}\text{sr}^{-1} = 2.402 \times 10^{-10}$ $\text{W m}^{-2}\text{sr}^{-1}$.) Measurement of the brightness were made at the regions labeled A through T in Figure 4.6 (labeled also on the contour plot of the Figure 4.7).

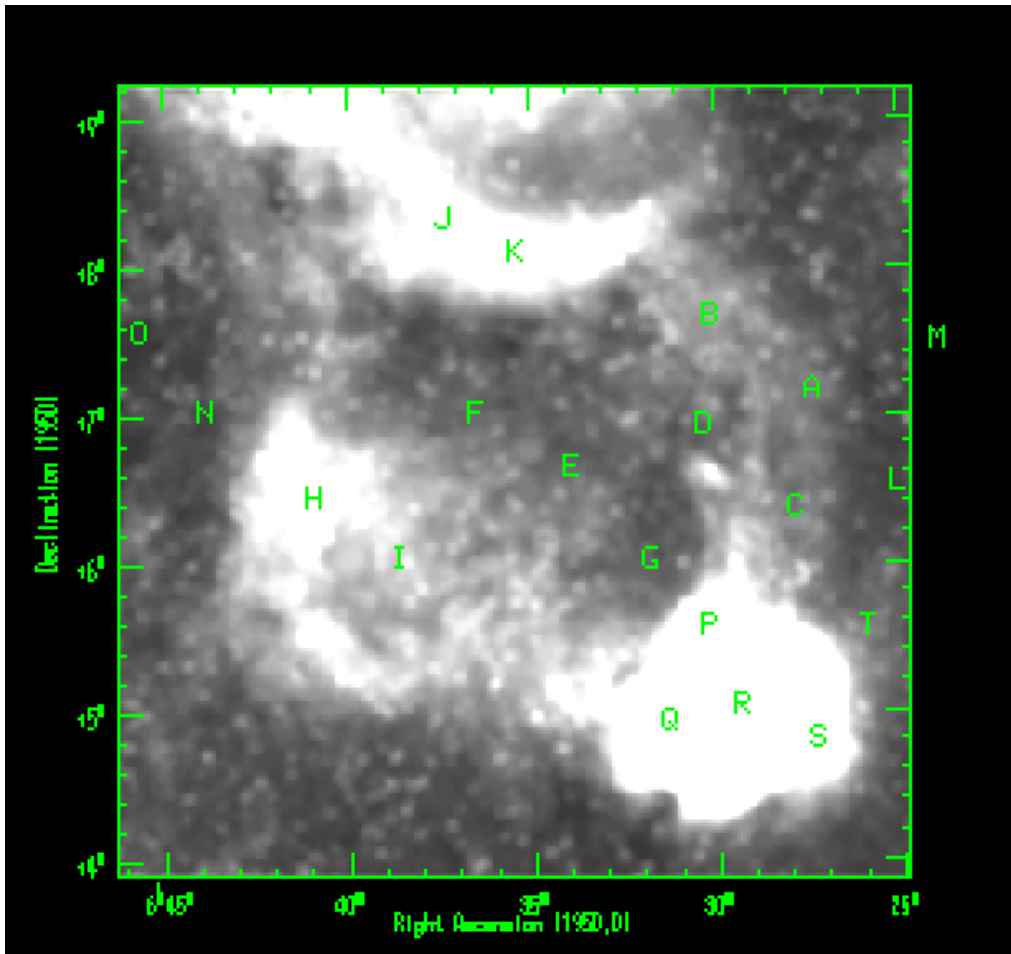


Figure 4.6 Total intensity $H\alpha$ image of the Monoceros supernova remnant (*center*), the Rosette Nebula (*lower right corner*), and the northern filament GS203+02-11 (*labeled by I, J, & K*). Letters refer to positions where the intensity was measured.

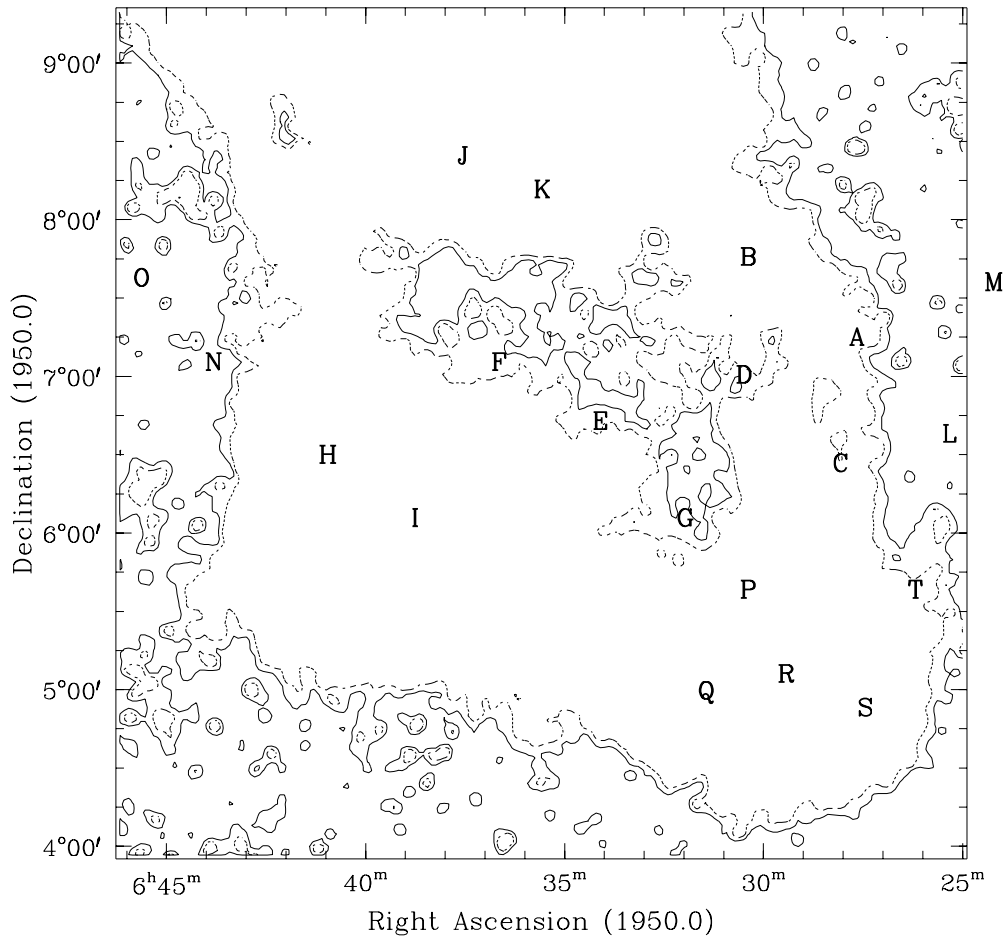


Figure 4.7 Contour plot of the total intensity H α image of the Monoceros supernova remnant (center), the Rosette Nebula (lower right corner), and the northern filament GS203+02-11 (labeled by I, J, & K). Letters refer to positions where the intensity was measured.

The intensity was measured by determining the mean and median inside a small 3×3 box at the various places labeled in Figure 4.6 and 4.15. The median and mean were practically the same, indicating that no bright pixels due to stars were dominant inside the box. The median for a pixel was recorded, a constant background subtracted, and the result divided by the integration time to normalize to one second. This number of counts was multiplied by the calibration constant K ($1.01 \times 10^{-8} \text{ W m}^{-2}\text{sr}^{-1}\text{count}^{-1}$) discussed in section 4.2 and then converted to Rayleighs using the value given previously. Table 4.2 lists the values of intensity observed in and around the supernova remnant. It shows that the emission from the supernova remnant is an order of magnitude smaller than for the Rosette Nebula.

Table 4.2
H α INTENSITIES AT THE LOCATION IN FIGURE 4.6 & 4.15

Location	Intensity (R)	Location	Intensity (R)
A	20	K	88
B	37	L	~ 0
C	20	M	5
D	10	N	1
E	15	O	~ 0
F	14	P	257
G	11	Q	507
H	98	R	501
I	51	S	214
J	99	T	26

The source of ionization in the ring is somewhat of a mystery. Graham (1982) points out that HD 48099, an O6 star about one-half a degree away from the center of expansion, is only marginally capable of ionizing the shell. He also points out that the situation is helped if the shell is either located closer to us or if it is elongated along the line of sight, however, evidence for the distance of the shell at ~ 1.5 kpc is convincing. I suggest that shock ionization may also play a role in the emission process. After the shock encounters the gas, it quickly raises its temperature and pressure. Any electrons behind the shock now have an increased temperature and, through collisions with other electrons, will thermalize the gas to some temperature T_e . Again, recombinations will occur with emission at discrete recombination wavelengths, of which H α is one of the wavelengths emitted. A shell-like structure of neutral hydrogen outside of the

optical filaments was detected by Riddle (1972). I believe we are seeing the photoionization of the interior of the shell by stellar UV flux from stars inside the remnant as well as a possible contribution to emission from shock ionization.

It is interesting to note that the brighter $H\alpha$ emission in Figure 4.6 (4.15) may actually be due to something else. One is the possibility that this region may itself be an HII region separate from the Monoceros supernova remnant. Graham (1982) showed that the peak in the 2700 MHz emission in this area has a thermal spectrum, suggesting it may be an HII region of its own. Clearly the $H\alpha$ emission is higher than in the western part of the shell, and as Table 4.2 shows, the emission is approximately ten times higher than in the fainter, more curved parts of the shell. Unless there is some sort of enhancement due to the supernova remnant in this region, it appears likely that the HII region labeled H in Figure 4.6 is separate, and possibly distinct, from the Monoceros supernova remnant. At the southern point of the remnant, and to the east of the Rosette Nebula, Celnik (1986) has shown that a region of high extinction exists by comparing radio continuum and $H\alpha$ observations. This extinction appears to cover a large region and does not seem to be correlated with the Rosette Nebula or the Monoceros supernova remnant.

Since an HI shell around the remnant has been identified by Riddle (1972), we might expect to see polarization by selective extinction of dust associated with the HI shell. However, like the northern filament possibly associated with GS203+02-11, the Monoceros supernova remnant shows no statistically significant polarization. Any of the possible reasons why no polarization was seen for the previous region can easily be applied here. Polarization of the $H\alpha$ emission is probably not seen because the emission is very weak. Even in the case of scattering, the emission is either too weak or the dust in the region is not efficient at scattering or selectively absorbing the radiation from the remnant. It should be pointed out however, that the western part of the remnant does appear in all four the IRAS bands, being particularly stronger at the $60 \mu m$ and $100 \mu m$ wavelengths. Still, regardless of this fact, no significant polarization is seen.

Various measurements of the velocity of expansion are about $\sim 45 \text{ km s}^{-1}$ and given the parameters of distance and radius, Graham (1982) calculates an age of about 1.5×10^5 years. Using the expansion velocity and age, Odegard (1986) calculates that for a release of 10^{51} ergs of energy, the ambient density is

0.34 cm^{-3} . This very small value of density may be another clue as to why we are not seeing polarization associated with the supernova remnant.

Taken together, the faintness of the shell in $\text{H}\alpha$, the low ambient density, polarization below the detection limit of the device, and possibly low polarization efficiency all seem like reasonable explanations of why polarization is not seen associated with the Monoceros supernova remnant. The only region which shows any significant polarization is the Rosette Nebula. As Figure 4.5 shows, the polarization is greatest in northwestern quadrant and appears patchy elsewhere in the nebula. Since this region shows significant polarization, we leave a full discussion and analysis for the remainder of this chapter. What has been shown in this section however, is the negative result of trying to detect polarization associated with two supernova remnants.

The Rosette Nebula

Of the three objects that were planned to be observed in the study, two (the Monoceros supernova remnant and the $\text{H}\alpha$ filament of GS203+02-11) showed no noticeable polarization which can be attributed to selective extinction due to aligned dust grains. Scattering is also not observed in any significant way, and what polarization there is associated with these two regions is probably a residual of background polarization. The Rosette Nebula, however, did show polarization that was statistically significant. As can be seen in Figure 4.5, the polarization in and around the Rosette Nebula is quite striking. It has an overall circular appearance at the outer edge of the nebula and a faint, patchiness in its interior. Since there is much to discuss about this region, the analysis of the polarization seen here will be the topic of the remainder of this chapter and presented more fully in the next two sections.

4.4 The Rosette Nebula

The Rosette Nebula is an HII region approximately 1.5° in angular diameter. Photometric observations by Ogura and Ishida (1981) and Perez et al. (1987) have determined the distance to the open cluster NGC 2244 which resides in the Rosette Nebula to be around 1.6 kpc. Associated with this cluster are 17 OB stars ranging from O4 to B3 which power the HII region. At the distance of 1.6 kpc, the nebula has a linear diameter of about 40 pc. The region is bright in $H\alpha$ as evidenced by the measured values in the nebula shown in Table 4.2 (section 4.3). The intensity reaches values on the order of ~ 500 Rayleighs in the brighter regions but tens of Rayleighs at the location of the cavity. This is to be expected since a spherical HII region with a central cavity would show an enhancement in emission as you look further away from the center toward the edge; the integrated emission along a path through the nebula to the observer increase. However, due purely to geometry, the path length would reach a maximum and then decrease. The nebular brightness, (see Figure 4.2, section 4.2), shows this expected behavior in that the brightness increases from the central cavity region, reaches a maximum, then falls off. The magnified $H\alpha$ image of the Rosette Nebula, Figure 4.9, reveals the well known central cavity which was remarked on by Menon (1962) as possibly resulting from the action of stellar winds. Later it was shown by Mathews (1966) that the central cavity of the Rosette Nebula could have been formed by the action of radiation pressure on dust grains in the nebula. This cavity is about $15'$ in diameter, and although generally circular, upon closer inspection reveals irregularities.

Figure 4.5 shows that a significant amount of polarization is seen in and around the Rosette Nebula. Figure 4.8 is an enlarged contour plot of the nebula with polarization vectors and Figure 4.9 is an enlarged total intensity image of the nebula which has been magnified in width and height to make it easier to see. Plotted polarization vectors were calculated using the γ trimmed mean method as were those in Figure 4.5. The γ trimmed mean was used since it is a robust statistic, insensitive to outliers. No measurements of intensity were made from this image.

Figure 4.8 shows that the polarization vectors form a circular pattern around the periphery of the nebula. All vectors are inside the 3σ contour line since the lowest cut for vectors was made at this level. That is to say, any pixel whose

total intensity was below the 3σ threshold did not have its polarization vector plotted. The largest break in the circular pattern occurs between the nine to twelve o'clock position. This also happens to be the location where the Monoceros supernova remnant appears to overlap the Rosette Nebula. As was mentioned in the previous section, decameter wavelength observations by Odegard (1986) indicate the Monoceros supernova remnant is behind the Rosette Nebula since non-thermal emission is absorbed by the Rosette Nebula. It seems reasonable to assume the influence of $H\alpha$ emission from the supernova remnant might be a cause of the low, almost absence, of polarization in this region due to dilution. However, there may not be a significant amount of dust in this region for polarization by scattering to be significant.

Comparing the IRAS $12\mu\text{m}$ emission with radio continuum at 4750 MHz mapped by Celnik (1985), Cox et al. (1990) have shown that very little $12\mu\text{m}$ emission is in the region where the Monoceros supernova remnant overlaps the Rosette Nebula. They also showed that $60\mu\text{m}$ emission is not very strong in the overlap region as well as the fact that CO ($J=1 \rightarrow 0$) emission mapped by Blitz and Thaddeus (1980) is weaker as well. The IRAS images map infrared emission from dust, and CO is a tracer of H_2 , which is generally believed to require dust as a catalyst for its formation in the interstellar medium. All these factors taken together, along with the near absence of high polarization, leads us to believe that dust is inconspicuous in the overlap region of the Rosette Nebula and the Monoceros supernova remnant. This would explain why polarization is practically absent in this region; there is hardly any dust in this region for polarization by scattering to be significant.

The interior shows polarization vectors which sometimes have directions in a pattern unrelated to an overall circular pattern at the perimeter of the nebula. Some of the smallest vectors show a tendency toward vertical alignment. Some of these are seen at around $6^{\text{h}} 32^{\text{m}}, 5^{\circ} 0'$. Their small magnitude and vertical tendency suggest that these are probably a residue of background polarization. Since a complete background subtraction is impossible with an image this large, some residue polarization is expected.

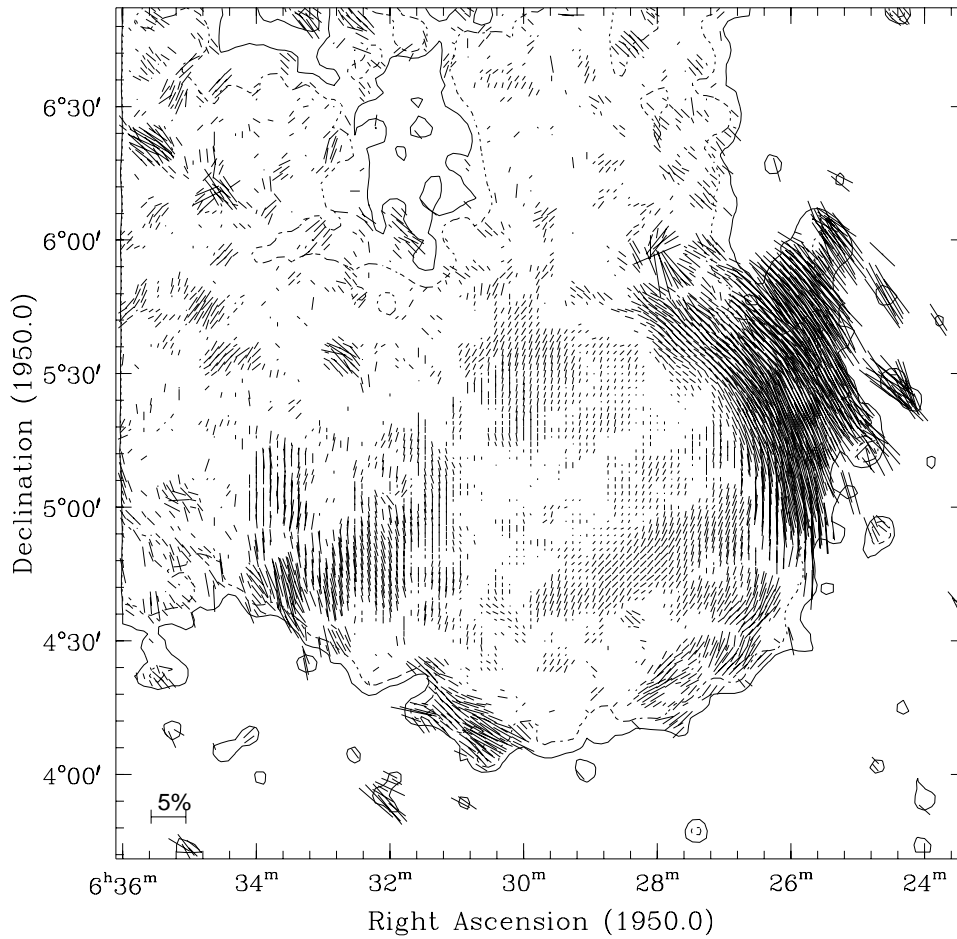


Figure 4.8 Contour plot of the Rosette Nebula with polarization vectors. The contours are 3σ (solid) and 5σ (dashed) above background. The polarization is seen to be circular in appearance with large ($> 1\%$) polarization seen at around the two o'clock position.

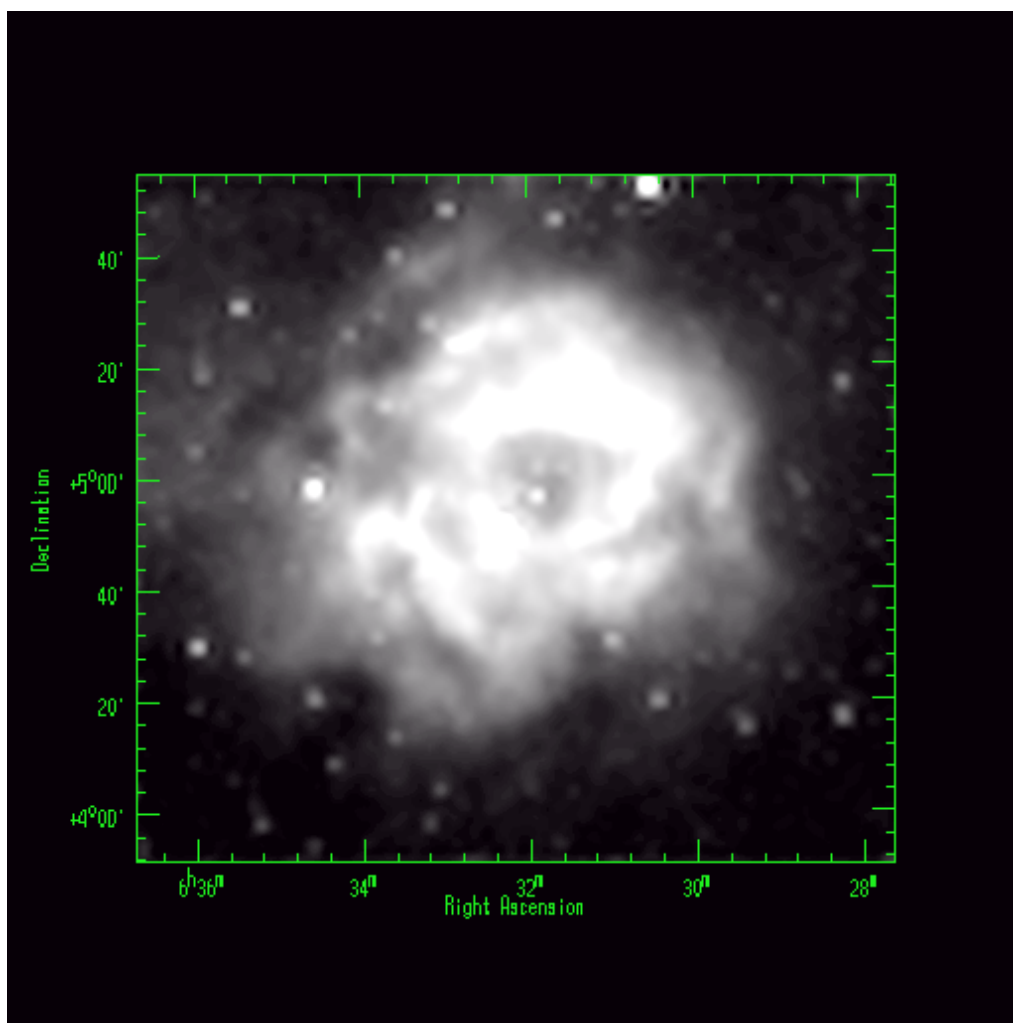


Figure 4.9 Total intensity $H\alpha$ image of the Rosette Nebula. The image has been magnified 4 times in both horizontal and vertical directions.

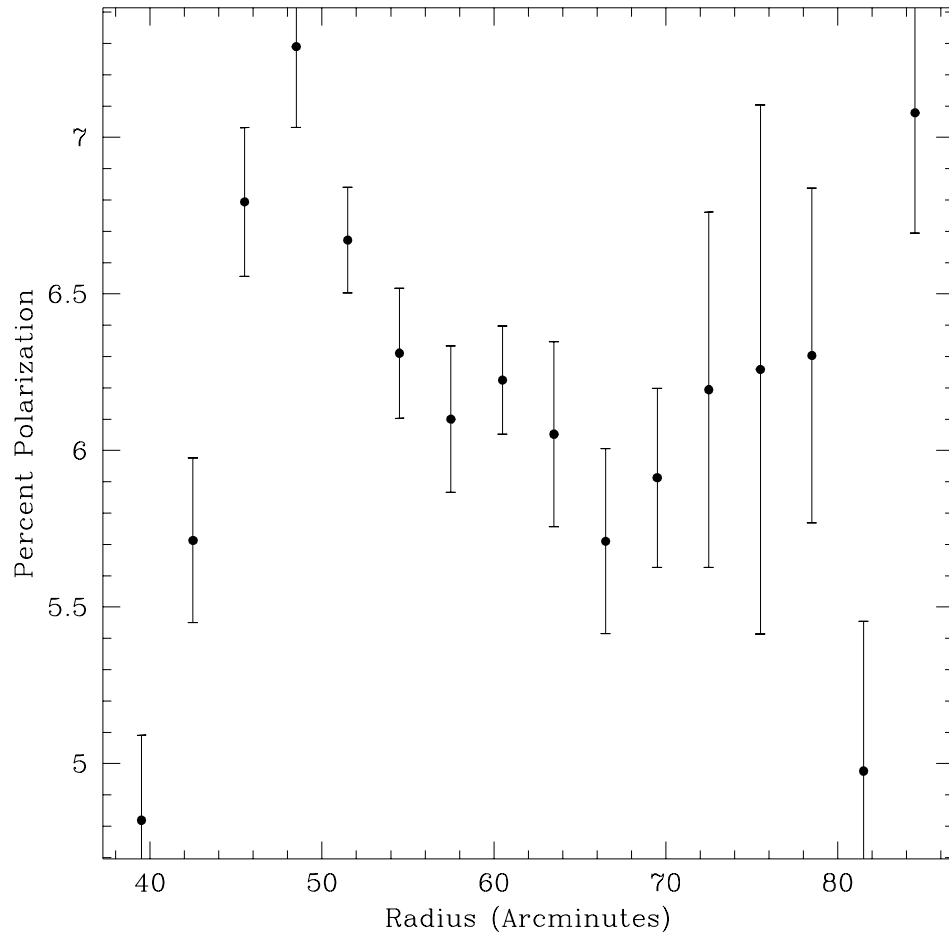


Figure 4.10 Average percent polarization as a function of radial distance from the HII region. Error bars are the standard deviation of the mean for mean values calculated in bin widths of 3.2' width.

Since the polarization vectors have a circular structure, it is reasonable to determine the degree of polarization as a function of radial distance from the center of the nebula. In his $H\alpha$ photometric map of the Rosette Nebula, Celnik (1983) found a central minimum located at $6^{\text{h}} 29^{\text{m}} 01^{\text{s}}.7$, $+5^{\circ} 00' 53''$ (1950.0). Later, 21 cm observations by Kuchar and Bania (1993) showed that the expansion center of an HI shell surrounding the Rosette Nebula was located at $6^{\text{h}} 29^{\text{m}} 8^{\text{s}}.67$, $5^{\circ} 0' 31''.9$ (1950.0) which is $1'.8$ from the central minimum found by Celnik. Therefore, I chose to take the center of the nebula to be the central minimum location found by Celnik (1983).

A plot of the degree of polarization as a function of radial distance from the center of the nebula is shown in Figure 4.10. This graph was created by averaging the polarization radially in bins of $3'.2$ in width from the center of the nebula. From this graph, it can be seen that the degree of polarization increases as the radial distance from the center increases, but quickly reaches a maximum and then begins to decline at about $48'$ but with variation at larger radii.

I mentioned observations by others which describe the Rosette Nebula as an overview and concentrated on describing the polarization associated with the Rosette Nebula. A possible cause of the polarization was suggested. I believe the polarization seen in the northwest region is due to scattering by dust grains. In the next section, evidence is presented which I feel supports this conclusion.

4.5 Polarization Analysis of Rosette Nebula

I shall attempt to explain the origin of polarization seen around the Rosette Nebula in this section. In doing so, we make use of the information presented in the previous section as well as data from other sources. I first present a case for polarization by scattering, suggesting that the polarization seen arises from scattering by dust grains outside the nebula and not by selective extinction. Next, a model based on Rayleigh scattering is derived to try and explain the observed polarization. It will be shown that this single scattering model is inadequate at predicting either the percent polarization or intensity at points outside the HII region. Finally, I present evidence which indicates that scattering is a likely scenario by showing a correlation between $H\alpha$ and infrared emission by dust as well as $H\alpha$ and [SII].

4.5.1 The Case for Polarization by Scattering

Section 4.4 dealt primarily with a description of the observed polarization seen around the Rosette Nebula. Briefly mentioned were observations of the region made by others. It was suggested that the observed polarization was probably caused by the scattering of $H\alpha$ emission by dust particles outside the HII region. In this section we take up this issue by presenting evidence which supports the scattering hypothesis. However, we must first consider the possibility that the polarization might be caused by selective extinction by elongated dust grains aligned with the magnetic field in the region of high polarization.

I address this question by relating the polarization observed to the maximum interstellar polarization observed in starlight as a function of reddening. In their study of the wavelength dependence of interstellar polarization, Serkowski et al. (1975) showed the existence of a correlation between observed polarization as function of color excess E_{B-V} (or reddening). Moreover, they showed that the maximum observed polarization is directly proportional to the color excess

$$P_{max}(\%) = 9.0 E_{B-V} \quad (4.8)$$

where E_{B-V} has units of magnitude.

I use this result to make a comparison between the observed degree of polarization in the Rosette Nebula and the upper limit predicted for the color excess. I do not have a measure of the color excess in this region, however, extinction in the Rosette Nebula at the wavelength of $H\alpha$ has been studied by Celnik (1986). Comparing $H\alpha$ with radio continuum observations, Celnik (1983, 1985), created a map of extinction across the Rosette Nebula. By converting the color excess into an expression of extinction, we can use the values of extinction from Celnik's map to determine the maximum observable degree of polarization in regions across the nebula.

The relationship between the magnitude difference in the visual band is related to the color excess by $a_\lambda = R_V E_{B-V}$ where R_V is the ratio of total to selective visual extinction. Substituting this into equation (4.8) we get

$$P_{max}(\%) = \frac{9.0}{R_V} a_\lambda \quad (4.9)$$

which relates maximum observed interstellar polarization to the optical extinction at wavelength λ and the ratio of total to selective visual extinction. Since we can obtain the extinction at the $H\alpha$ wavelength from Celnik (1986), we only need to determine the ratio of total to selective visual extinction. R_V is an observationally obtained quantity which is expected to depend on grain composition and size distribution. In the low density of the interstellar medium, however, the value of R_V is found to be nearly a constant value of $R_V \sim 3.05 \pm 0.15$ (Whittet 1992). Values of R_V for NGC 2244 have been determined by Perez et al. (1987) and Ogura and Ishida (1981) of 3.1 and 3.2 ± 0.1 respectively. Using this latter value of R_V , we find that

$$P_{max}(\%) = (2.8 \pm 0.1)a_\lambda. \quad (4.10)$$

From the map by Celnik (1986), the optical depth at $H\alpha$ wavelength in the Rosette Nebula close to the region of high scattering has a minimum value of 1.1 ± 0.3 magnitudes. Equation (4.10) implies that the polarization observed in this region should be no greater than 3.1 ± 0.3 percent. North of the nebula center the optical depth has a mean value of 1.4 ± 0.1 magnitudes, implying a maximum polarization of 3.9 ± 0.1 percent. Celnik (1986) points out that the $H\alpha$ measurements contain a small amount of optical continuum radiation from the Rosette Nebula itself and that the values of optical depth are at least upper limits.

From the argument presented above we find that, at the wavelength of $H\alpha$, the maximum observed polarization near the region of high polarization should be no greater than 3% to 4%. If we can extrapolate this into the region of high polarization, we see that the maximum observed polarization of $\sim 10\%$ is a factor of ~ 3 times higher than expected. From this we conclude that polarization resulting from align dust grains is not likely the cause of the observed polarization.

We also need to consider the possibility that polarization may be caused by scattered starlight, i.e. light from the central cluster is scattered by dust grains at the periphery of the HII region. This could also be the cause the high degree of linear polarization since reflection nebulae are generally known to have a high degree of polarization. Since the brightest of the stars in the stellar cluster NGC 2244 are visible in the total intensity image at the $H\alpha$ wavelength, we want to determine if scattered flux from these stars is the cause of the high degree of polarization. That is, if the flux from the stellar cluster in the $H\alpha$ bandpass $F_{H\alpha}$

produces an intensity $I_{H\alpha}$ at the region of high polarization, then is what we are seeing polarization by this scattered stellar flux? We can answer this question with the following argument.

Suppose the continuum flux from the stellar cluster is F_C and the corresponding intensity at the region of high polarization is I_C . Then by comparing $F_{H\alpha}$ and $I_{H\alpha}$ we should find that the ratio of I_C to F_C should be similar to the ratio of $I_{H\alpha}$ to $F_{H\alpha}$. That is

$$\frac{I_{H\alpha}}{F_{H\alpha}} \sim \frac{I_C}{F_C} \quad (4.11)$$

where the equality of ratios is not strict since the process depends on radiative transfer through the nebula at two different but nearby wavelengths as well as reflection at two different wavelengths. However, this will at least give us a measure of what the predicted $H\alpha$ intensity should be at the location of scattering.

In order to determine the expected scattered $H\alpha$ intensity, $H\alpha$ and continuum images were obtained from the $H\alpha$ sky survey. The continuum images were obtained using a wide bandpass (8 nm) interference filter with center wavelength 608.3 nm which is in a line-free part of the spectrum. The brightest of the central stars in the Rosette Nebula are visible in both the $H\alpha$ and continuum images and so a measurement of their fluxes were made. Since the pixel size is $1''.6$, the stellar cluster is only partially resolved; the stars appear as an irregularly shaped, smeared out distribution. Nevertheless, the photometry was performed by measuring counts inside a rectangular aperture centered so that most of the pixels associated with the cluster were in the aperture. The $H\alpha$ and continuum fluxes measured were 65,900 and 459,700 counts respectively. (Backgrounds were obtained in regions close to the cluster where the intensity was lower, and subtracted from the flux counts.) The intensity was then measured in the region where the polarization reaches it highest value ($\sim 10\%$) in both the $H\alpha$ and continuum images using a smaller 3×3 box, being careful to avoid stars and using the same location in the two images. A background was found and subtracted from the measured emission resulting in 74 and 809 counts per pixel in intensity for the continuum and $H\alpha$ images respectively. Therefore, using equation (4.11), the predicted $H\alpha$ intensity,

$$I_{H\alpha}^P \sim I_C \frac{F_{H\alpha}}{F_C} \quad (4.12)$$

is 11 counts per pixel. Thus, if the light from the stellar cluster at the $H\alpha$ wavelength is responsible for the polarization by scattering seen, then only 11 counts in each pixel are available to produce polarization assuming 100% efficiency of scattering at the $H\alpha$ wavelength. However, since we observe 10% polarization at the location measured, then the number of counts which are polarized is $0.10I_{H\alpha} = 81$ counts per pixel (where $I_{H\alpha}$ is the 809 counts per pixel that were observed). Therefore, we see eight times more polarization than expected by scattered light from the stellar cluster alone.

Because of the Rosette Nebula's spherical nature, $H\alpha$ undoubtedly exist in front of and behind the stellar cluster. Thus, the measurement of the $H\alpha$ stellar flux is probably overestimated. Likewise, using a 12×13 rectangular aperture to measure the flux from the cluster incorporates a few background pixels, making its value only slightly larger. Therefore, the predicted $H\alpha$ intensity of 11 counts per pixel from equation 4.12 is an upper limit to the number of counts in each pixel available to produce polarization. Also, given that 100% scattering efficiency is unlikely, we can rule out the possibility that the observed polarization is due to scattered starlight from the central cluster at the $H\alpha$ wavelength. Therefore, I conclude that the source of light that is scattered is $H\alpha$ emission from the Rosette Nebula.

The Cygnus region was targeted for study for two reasons. The first is that NGC 7000, the North America Nebula, was observed as a test region. Before the building of the rotating polarizer device used in this project, a test to see if polarization could be observed was made by imaging the North America Nebula. A simple rotating polarizer which attaches to the front of a 52 mm camera lens was used for the test. The polarizer was marked at every 45° around its perimeter and installed by attaching it to the camera lens. The polarizer was rotated by hand and images obtained at every 45° angle. Stokes I , Q , and U images were created in the manner described in this project as well as polarization maps. Observing the region again with the rotating polarizer device built for this project provided a consistency check. Both images were very similar in the location of where polarization was seen.

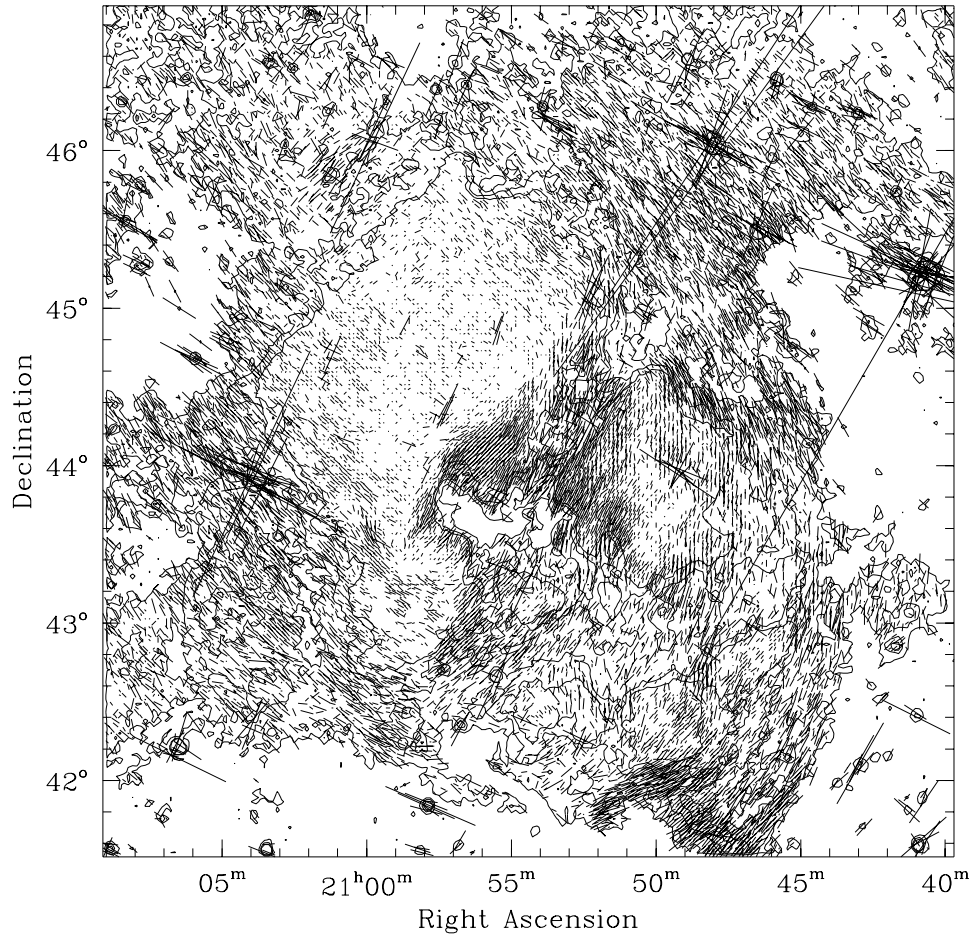


Figure 4.11 Contour plot with polarization vectors of the North America Nebula (NGC 7000).

Secondly, the Cygnus region appears to contain large shells as well as the Cygnus loop. These were imaged and it was hoped they would show polarization vectors aligned with the emission and filaments of the shells. These images have not been analyzed in detail due to the complexity of the region. However, we present in Figure 4.11 the contour plot and polarization image of the North America Nebula obtained in this project. This image clearly shows that polarization is ubiquitous across the region. The curved nature of the polarization vectors around the North America Nebula suggest two possibilities; 1) they are due to selective extinction by elongated dust grains aligned with the magnetic field in the region, or 2) they are produced by scattering from dust particles close to the nebula. We favor the latter interpretation since the polarization is generally perpendicular to the line of sight for the bright HII region. On the other hand the former interpretation requires the magnetic field to be quite erratically curved.

We now look at published data and combine it with our own to strengthen the case for polarization by scattering. As was mentioned in section 4.4, from the analysis of IRAS observation and other data, Cox et al. (1990) showed that the infrared emission obtained by the IRAS satellite was unevenly distributed throughout the Rosette Nebula. The $12\mu\text{m}$ and $60\mu\text{m}$ emission is weak in the region where the Monoceros supernova and the Rosette Nebula overlap. Likewise, the CO ($J = 1 \rightarrow 2$) emission isn't as prevalent in this region either. We interpreted this as an indication of the absence of a significant amount of dust in this region and hence polarization by scattering is very small. We revisit the question of scattering by dust by relating the $H\alpha$ intensity in the region of high polarization to infrared emission in section 4.5.4

There are also observations in HI which relate well to the scattering interpretation. An HI shell around the Rosette Nebula has been mapped by Menon (1962) and Davies et al. (1963) but at low resolution. Kuchar and Bania (1993) have mapped 8.4 square degrees of the Rosette complex at a high resolution at 21 cm wavelength. Taking the radius of $38'$ as it appears on the POSS* red plate, they find that the HII region to be surrounded by three dense HI regions which are part of a shell of HI which surrounds the entire HII region. While the HI shell exhibits an elliptical nature, its deviation from non-circularity is not extreme. Kuchar and Bania find that the interior of the shell is

*Palomar Sky Survey

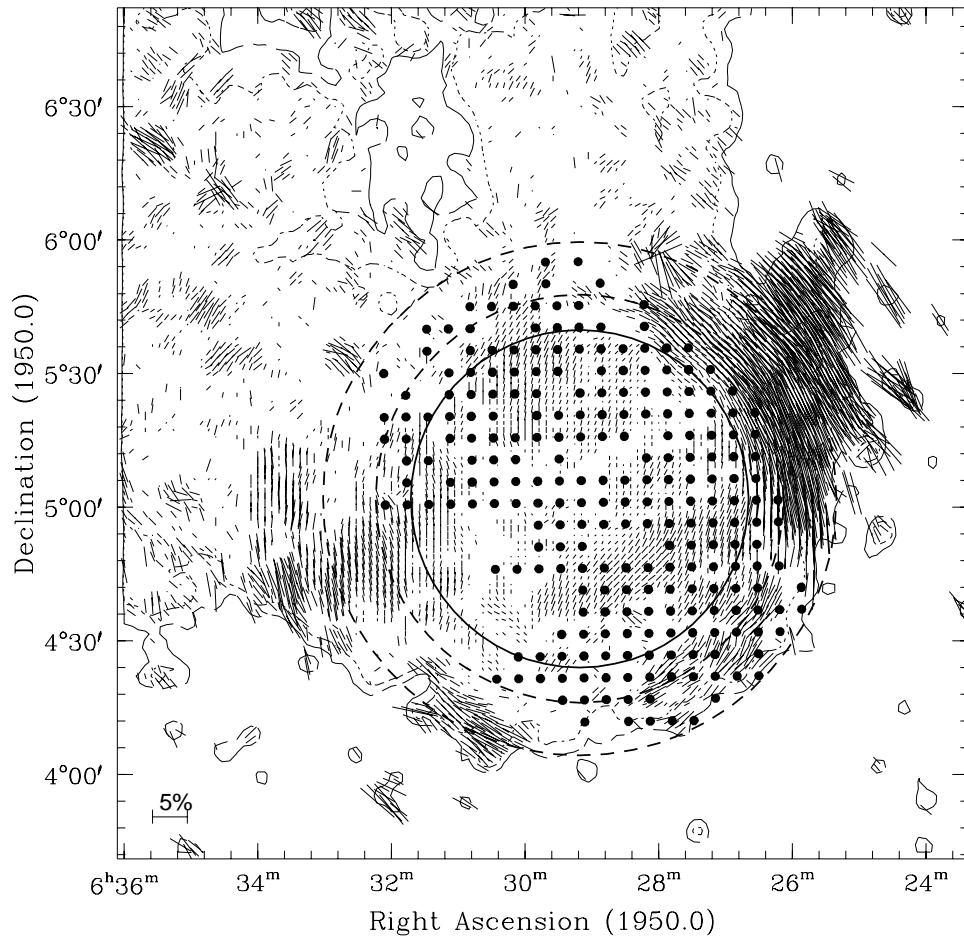


Figure 4.12 Contour plot of the Rosette Nebula with polarization vectors. The interior circle marks the rough interior of an HI shell mapped by Kuchar and Bania (1993) as well as their determination of the nebula's extent from the POSS red plate. The two outer circles roughly indicate the radii of the shell which varies in thickness.

$0.64^\circ = 38'.4$ in radius from the expansion center. The interior edge of the HI shell is close to the $H\alpha$ minimum in the direction of high polarization. This is shown in Figure 4.12 which shows the interior radius of the HI shell marked by the smaller heavy circle. Points locating radio continuum emission observed on Celnik's (1985) continuum map are indicated by heavy dots. The absence of heavy dots towards the region of high scattering is due to the fact that no continuum emission was recorded on his published map. The continuum emission ends about where the HI shell begins. While Kuchar and Bania point out that the shell varies in thickness from $8'$ to $20'$, it is interesting to note that the larger thickness corresponds well with the 3σ perimeter of the $H\alpha$ contour in the southeast region of the nebula.

The location of one of the maxima in the velocity integrated HI intensity image roughly corresponds to the location of maximum polarization seen by our image. Other regions of high HI intensity appear to the south and south east. In the velocity integrated map by Kuchar and Bania, the HI emission in the southern part does appear to be generally less than either of the two previously mentioned regions. The region toward the southeast appears to extend farther than the other two regions as well, seeming to indicate a possible relationship to the region of high extinction seen in the southeast by Celnik (1986). Regions to the north and northeast generally appear to have lower values of velocity integrated HI as well. The region to the northwest corresponds well with the lower part of the region of high polarization, the absence of strong, coherent polarization in the south and southeast is, we believe, explained by the following. In his analysis of dust extinction in the Rosette Nebula, Celnik (1986) showed that the south and southeast regions of the Rosette Nebula exhibited high extinction. In fact, from his map of optical depth, the southwestern region is the region of maximum extinction around 4 magnitudes. The extinction in the third quadrant of the nebula is generally high as well by inspection of the optical depth map. We believe this high extinction to be the reason we are not seeing polarization as high as in the other region where extinction is a minimum.

The evidence presented in this section leads me to believe that scattering is the most likely cause of the polarization we observe. I have shown that the polarization is not caused by selective extinction, but rather by scattered $H\alpha$ starlight. HI maps show that regions of enhanced atomic hydrogen roughly correspond to the region of high polarization. I now look at the question more

quantitatively by developing a single scattering model based on Rayleigh scattering to try and describe the degree of polarization observed.

4.5.2 The Single Scattering Model

In this section we develop a model to describe the observed polarization from the Rosette Nebula. The foundation of the model is based on the idea that $H\alpha$ light from the nebula is Rayleigh scattered from dust grains surrounding the nebula. It assumes the nebula is spherically symmetric and that Rayleigh scattering from dust particles whose size is small compared to the wavelength of $H\alpha$ light is responsible for the observed intensity and polarization. These are the only assumptions built into the model which predicts the percent polarization and intensity for a particular line of sight near the nebula.

The scattering model is laid out in Figure 4.13. We want to know the intensity of a scattered ray at some point P outside the nebula as shown in Figure 4.13 due to all of the light from the assumed spherically symmetric nebula. Figure 4.13 shows one particular ray from the nebula arriving at point P and scattering toward the earth. Our model requires a knowledge of the intensity at the scattering point for any particular ray from the nebula

The time independent equation of radiative transfer, which describes the change in intensity for a ray propagating in the \hat{k}_o direction which undergoes absorption, scattering, and emission is

$$\hat{k}_o \cdot \nabla I_\nu = \frac{1}{4\pi} \rho j_\nu + \rho \kappa_\nu^{sca} \oint \phi(\hat{k}, \hat{k}') I_\nu(\hat{k}') d\Omega' - \rho \kappa_\nu^{abs} I_\nu - \rho \kappa_\nu^{sca} I_\nu \quad (4.13)$$

where I_ν is the specific intensity, ρ is the mass density per unit volume of the gas, j_ν its emissivity per unit mass, κ_ν^{sca} its total scattering opacity, κ_ν^{abs} the total absorption opacity of the gas. The first term represents intensity added to the beam due to emission and the second due to scattering into the beam. The last two terms represent absorption and scattering out of the beam.

I am first going to solve for the intensity along a ray through the nebula. The intensity along a ray needs to be determined so that the intensity at the scattering point P due to the integrated emission from the nebula is known. Consider the case where scattering into and out of the beam, as well as absorption, do not occur. If we take the change in intensity to be solely along the ray, then equation

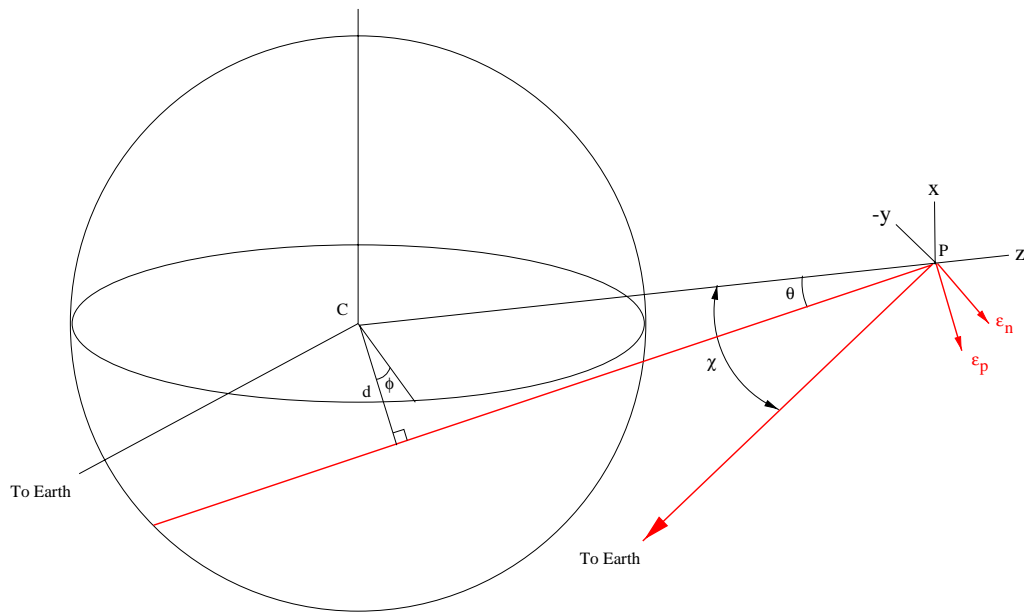


Figure 4.13 Geometry of the scattering model developed in this section to explain the observed polarization and intensity from the Rosette Nebula

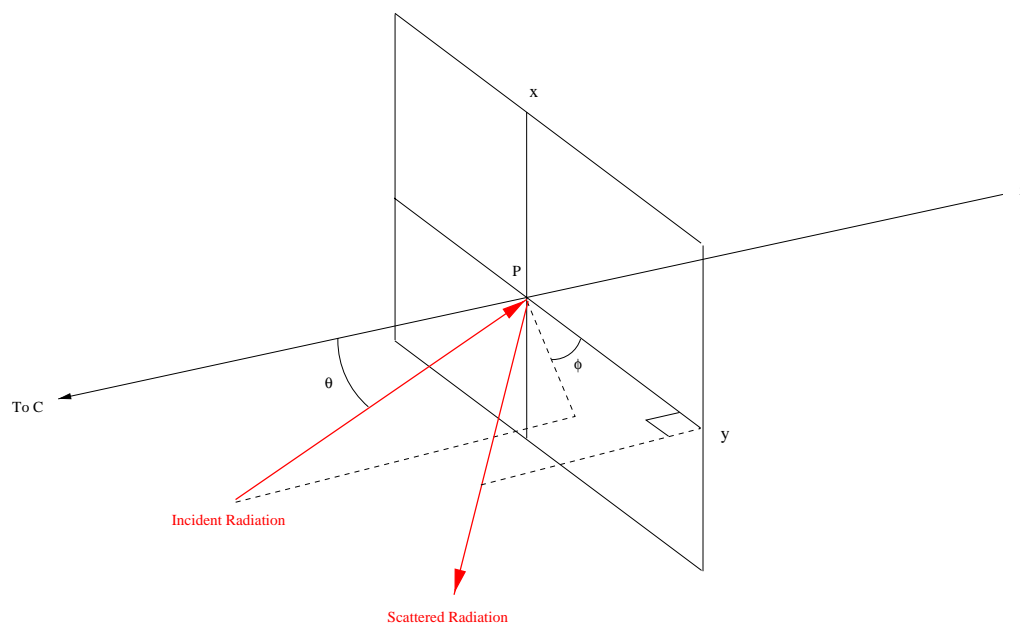


Figure 4.14 The Cartesian coordinate system and the relationship between the incident and scattered rays at the scattering point.

(4.13) reduces to

$$\frac{dI_\nu}{ds} = \frac{1}{4\pi} \rho j_\nu = J_\nu \quad (4.14)$$

where J_ν is the energy emitted into the beam per cubic centimeter per second per steradian. Equation (4.14) can be integrated to yield

$$I_\nu = \int_{s_1}^{s_2} J_\nu ds \quad (4.15)$$

which is the intensity at some particular point due to the integrated emission along a ray to that point. As shown in Figure 4.13, we need the intensity at point P from along a ray through the nebula. If one knows the functional form of J_ν then the integral in equation (4.15) can be evaluated. However, we can arrive at the intensity at point P which is due to the integrated emission along the ray without having any particular knowledge of J_ν by the following method.

Consider the observation of the nebula itself. Any ray leaving the nebula has an observed intensity I_ν which is due to the integrated emission along the line of sight through the nebula, assuming of course that no absorption or scattering into or out of the beam occurs en route to the observer. We shall make this assumption and say that the observed intensity distribution is due solely to emission from the Rosette Nebula itself. Let the observed line of sight through the nebula be a perpendicular distance d from the center of the nebula. We can then create a map of the intensity as a function of d . Then, as shown in Figure 4.13, any ray which makes an angle θ with respect to the center of the nebula can be related to a particular observed intensity which is a perpendicular distance d from the nebula's center. It is by this method that we shall determine the intensity at point P rather than by equation (4.15).

Now that the intensity at the scattering point P can be determined, we need a model that describes the scattered intensity directed toward the observer at that point. We set up a coordinate system at the scattering point as shown in Figure 4.14 and Figure 4.15. Since the intensity at point P depends on the angle made with respect to the Cartesian axes shown, we shall denote the intensity at point P by $I'_\nu(\theta, \phi)$. The incident ray then forms a plane determined by the line \overline{PC} and the incident ray and is called the incident plane. The radiation is scattered at

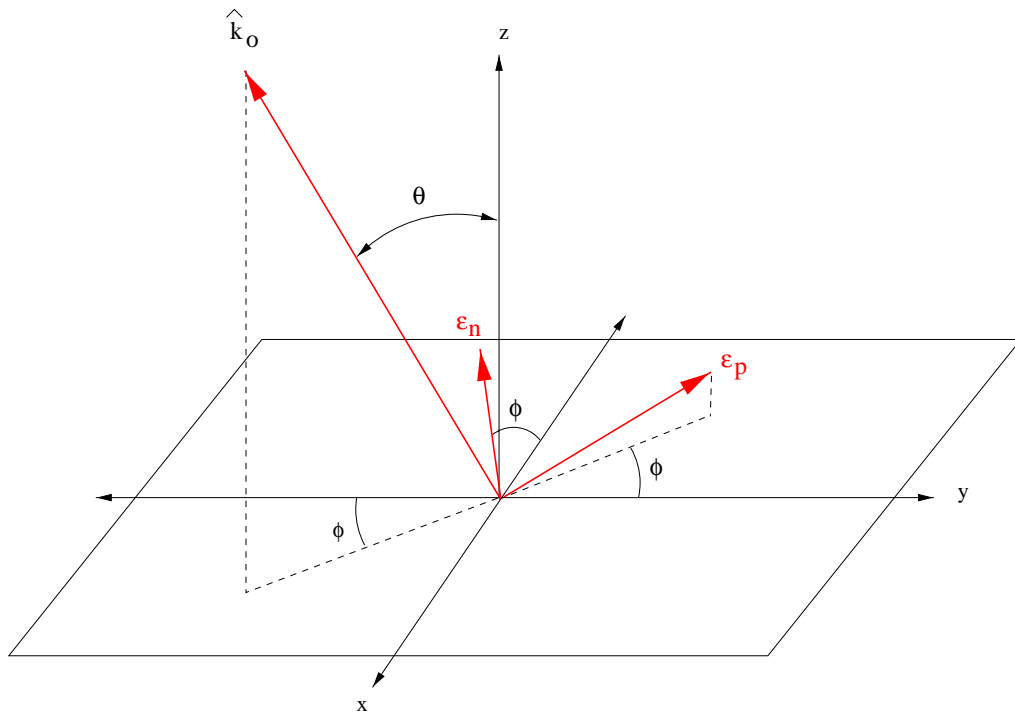


Figure 4.15 Scattering of incident radiation propagating in the \hat{k}_o direction. The incident ray is resolved into two orthogonal components ϵ_p and ϵ_n both of which are perpendicular to \hat{k}_o . ϵ_p lies in the incident plane.

an angle χ with respect to the line \overline{PC} and the scattered ray lies in the y - z plane as shown in Figure 4.14. Likewise, the center of the nebula and the earth lie in the y - z plane as well. We shall call the y - z plane the scattering plane.

In the model we are assuming that the scattered radiation results from Rayleigh scattering from a dust particle. We shall assume that there is no appreciable amount of interaction between dust grains or possibly from any other surrounding particles. This is a reasonable assumption since the number density of particles in the interstellar medium is generally very low. As the electromagnetic wave interacts with the dust grain it induces a dipole moment in the dust grain. If the electrons in the dust grain are bound by a linear restoring force $\gamma\vec{r}$, and if damping is neglected, then the equation of motion for a single electron with charge e and mass m is

$$m \frac{d^2\vec{r}}{dt^2} + \gamma\vec{r} = e\vec{E}(\vec{x}, t) \quad (4.16a)$$

or,

$$\frac{d^2\vec{r}}{dt^2} + \omega_o^2\vec{r} = \frac{e}{m}\epsilon_o E_o e^{i(\hat{\mathbf{k}}_o \cdot \vec{r} - \omega t)} \quad (4.16b)$$

where $\omega_o = \sqrt{\gamma/m}$ is the resonant frequency, and the electric field with propagation vector $\hat{\mathbf{k}}_o$ and polarization vector ϵ_o is $\vec{E}(\vec{x}, t) = \epsilon_o E_o e^{i(\hat{\mathbf{k}}_o \cdot \vec{r} - \omega t)}$. The solution to equation (4.16) is

$$\vec{r}(t) = \frac{(e/m)}{\omega_o^2 - \omega^2} \epsilon_o E_o e^{i(\hat{\mathbf{k}}_o \cdot \vec{r} - \omega t)}. \quad (4.17)$$

Now the instantaneous power radiated into a polarization state ϵ and into a solid angle Ω by a charge e at low velocities is given by Jackson (1975) as

$$\frac{dP}{d\Omega} = \frac{e^2}{4\pi c^3} |\epsilon^* \cdot \ddot{\vec{r}}|^2 \quad (4.18)$$

where $\ddot{\vec{r}}$ is the second derivative of the displacement vector with respect to time. Rather than the instantaneous power radiated we need the time-averaged power

radiated into a solid angle which is

$$\left\langle \frac{dP}{d\Omega} \right\rangle = \frac{e^2}{4\pi c^3} \left\langle |\boldsymbol{\epsilon}^* \cdot \ddot{\mathbf{r}}|^2 \right\rangle. \quad (4.19)$$

The time average of $|\ddot{\mathbf{r}}|^2$ equals $\frac{1}{2} \text{Re}(\ddot{\mathbf{r}} \cdot \ddot{\mathbf{r}}^*)$ so long as the electron moves only a negligible part of a wavelength during an oscillation, Jackson (1975). Taking the second derivative of equation (4.17) with respect to time (and using the fact above) equation (4.19) yields an expression for the time average power radiated into a solid angle as

$$\left\langle \frac{dP}{d\Omega} \right\rangle = \frac{c}{8\pi} |E_o|^2 \left(\frac{e^2}{mc^2} \right)^2 \left[\frac{\omega^2}{\omega_o^2 - \omega^2} \right]^2 |\boldsymbol{\epsilon}^* \cdot \boldsymbol{\epsilon}_o|^2. \quad (4.20)$$

In equation (4.20) we note that $c|E_o|^2/8\pi$ is the incident energy flux which is the time-averaged Poynting vector $\langle \vec{\mathcal{S}} \rangle$ and that (e^2/mc^2) is the expression for the classical radius of the electron. Now the time-averaged power radiated into a solid angle is related to the incident energy flux and differential cross-section $d\sigma/d\Omega$ by

$$\left\langle \frac{dP}{d\Omega} \right\rangle = \langle \vec{\mathcal{S}} \rangle \left\langle \frac{d\sigma}{d\Omega} \right\rangle \quad (4.21)$$

which indicates that the differential cross-section is, by equation (4.20), given by

$$\frac{d\sigma}{d\Omega} = \left(\frac{e^2}{mc^2} \right)^2 \left[\frac{\omega^2}{\omega_o^2 - \omega^2} \right]^2 |\boldsymbol{\epsilon}^* \cdot \boldsymbol{\epsilon}_o|^2. \quad (4.22)$$

Now the differential cross-section has units of area per steradian. Since $(e^2/mc^2)^2$ has units of area, and $[\omega^2/(\omega_o^2 - \omega^2)]^2$ is unitless, we can rewrite equation (4.22) as

$$\frac{d\sigma}{d\Omega} = \sigma |\boldsymbol{\epsilon}^* \cdot \boldsymbol{\epsilon}_o|^2 \quad (4.23)$$

where σ is a cross-section with units of area. Therefore, equation (4.21) can be written as

$$\left\langle \frac{dP}{d\Omega} \right\rangle = \langle \vec{\mathcal{S}} \rangle \sigma |\boldsymbol{\epsilon}^* \cdot \boldsymbol{\epsilon}_o|^2 \quad (4.24)$$

and finally in terms of intensities as

$$I(\theta, \phi) = I'_\nu(\theta, \phi) \sigma |\boldsymbol{\epsilon}^* \cdot \boldsymbol{\epsilon}_o|^2 \quad (4.25)$$

where $I'_\nu(\theta, \phi)$ is the incident intensity and $I(\theta, \phi)$ the scattered intensity.

Now by using equation (4.25), for a particular incident polarization state $\boldsymbol{\epsilon}_o$ and incident intensity $I'_\nu(\theta, \phi)$, we can determine the scattered intensity $I(\theta, \phi)$ of any particular scattered polarization state $\boldsymbol{\epsilon}^*$. In particular we will want to know the two scattered polarization states which are mutually orthogonal and perpendicular the scattered ray.

Since the incident light is assumed to be unpolarized, it can be resolved into two orthogonal components which are denoted by the unit vectors $\boldsymbol{\epsilon}_p$ and $\boldsymbol{\epsilon}_n$ as shown in Figure 4.15. The unit vector $\boldsymbol{\epsilon}_p$ is perpendicular to the incident radiation and lies in the incident plane. The other vector is also perpendicular to the incident radiation and lies in the x - y plane. The incident ray propagating in the $\widehat{\boldsymbol{k}}_o$ direction and its two orthogonal components $\boldsymbol{\epsilon}_p, \boldsymbol{\epsilon}_n$ shown in Figure 4.15 are described by the vectors

$$\widehat{\boldsymbol{k}}_o = \sin \theta \sin \phi \widehat{\boldsymbol{e}}_x - \sin \theta \cos \phi \widehat{\boldsymbol{e}}_y + \cos \theta \widehat{\boldsymbol{e}}_z \quad (4.26)$$

$$\boldsymbol{\epsilon}_p = -\cos \theta \sin \phi \widehat{\boldsymbol{e}}_x + \cos \theta \cos \phi \widehat{\boldsymbol{e}}_y + \sin \theta \widehat{\boldsymbol{e}}_z \quad (4.27)$$

$$\boldsymbol{\epsilon}_n = -\cos \phi \widehat{\boldsymbol{e}}_x - \sin \phi \widehat{\boldsymbol{e}}_y \quad (4.28)$$

which can easily be shown to satisfy the orthogonality conditions $\boldsymbol{\epsilon}_p \cdot \boldsymbol{\epsilon}_n = \boldsymbol{\epsilon}_p \cdot \widehat{\boldsymbol{k}}_o = \boldsymbol{\epsilon}_n \cdot \widehat{\boldsymbol{k}}_o = 0$.

Since the scattered radiation is in the y - z plane, but at an angle χ with respect to the line \overline{PC} as shown in Figure 4.14, the two mutually orthogonal unit polarization vectors which are perpendicular to the propagation direction of the scattered radiation are

$$\boldsymbol{\epsilon}_\perp^* = \widehat{\boldsymbol{e}}_x \quad (4.29a)$$

$$\boldsymbol{\epsilon}_\parallel^* = \cos \chi \widehat{\boldsymbol{e}}_y + \sin \chi \widehat{\boldsymbol{e}}_z \quad (4.29b)$$

where $\boldsymbol{\epsilon}_\perp^*$ is the polarization vector perpendicular to the scattering plane and $\boldsymbol{\epsilon}_\parallel^*$ is the polarization vector in the scattering plane. From equation (4.23) we can

determine the differential cross-sections for two mutually orthogonal polarization states of the scattered radiation. The differential cross-sections corresponding to these states of scattered polarization are

$$\left. \frac{d\sigma}{d\Omega} \right|_{\epsilon_x^* \cdot \epsilon_p} = \sigma \left| \widehat{\epsilon}_x \cdot \epsilon_p \right|^2 = \sigma \cos^2 \theta \sin^2 \phi \quad (4.30a)$$

$$\left. \frac{d\sigma}{d\Omega} \right|_{\epsilon_y^* \cdot \epsilon_p} = \sigma \left| \cos \chi \widehat{\epsilon}_y \cdot \epsilon_p \right|^2 = \sigma \cos^2 \chi \cos^2 \theta \cos^2 \phi \quad (4.30b)$$

$$\left. \frac{d\sigma}{d\Omega} \right|_{\epsilon_z^* \cdot \epsilon_p} = \sigma \left| \sin \chi \widehat{\epsilon}_z \cdot \epsilon_p \right|^2 = \sigma \sin^2 \chi \sin^2 \theta \quad (4.30c)$$

$$\left. \frac{d\sigma}{d\Omega} \right|_{\epsilon_x^* \cdot \epsilon_n} = \sigma \left| \widehat{\epsilon}_x \cdot \epsilon_n \right|^2 = \sigma \cos^2 \phi \quad (4.30d)$$

$$\left. \frac{d\sigma}{d\Omega} \right|_{\epsilon_y^* \cdot \epsilon_n} = \sigma \left| \cos \chi \widehat{\epsilon}_y \cdot \epsilon_n \right|^2 = \sigma \cos^2 \chi \sin^2 \phi \quad (4.30e)$$

$$\left. \frac{d\sigma}{d\Omega} \right|_{\epsilon_z^* \cdot \epsilon_n} = \sigma \left| \sin \chi \widehat{\epsilon}_z \cdot \epsilon_n \right|^2 = 0 \quad (4.30f)$$

Combining the differential cross-sections given by equations (4.30a...f) which are in the same direction we obtain

$$\left. \frac{d\sigma}{d\Omega} \right|_{\perp} = \left. \frac{d\sigma}{d\Omega} \right|_{\epsilon_x^* \cdot \epsilon_p} + \left. \frac{d\sigma}{d\Omega} \right|_{\epsilon_x^* \cdot \epsilon_n} = \sigma (\cos^2 \theta \sin^2 \phi + \cos^2 \phi) \quad (4.31a)$$

$$\begin{aligned} \left. \frac{d\sigma}{d\Omega} \right|_{\parallel} &= \left. \frac{d\sigma}{d\Omega} \right|_{\epsilon_y^* \cdot \epsilon_p} + \left. \frac{d\sigma}{d\Omega} \right|_{\epsilon_y^* \cdot \epsilon_n} + \left. \frac{d\sigma}{d\Omega} \right|_{\epsilon_z^* \cdot \epsilon_p} + \left. \frac{d\sigma}{d\Omega} \right|_{\epsilon_z^* \cdot \epsilon_n} \\ &= \sigma \left[\cos^2 \chi (\cos^2 \theta \cos^2 \phi + \sin^2 \phi) + \sin^2 \chi (\sin^2 \theta) \right]. \quad (4.31b) \end{aligned}$$

Equations (4.31a) and (4.31b), combined with equations (4.23) and (4.25) yield

the intensity of the scattered radiation polarized perpendicular and parallel to the scattered ray. Therefore, the intensity of the scattered radiation with polarization perpendicular to the scattering plane is given by the expression

$$I_{\perp}(\theta, \phi, \chi) = \sigma I'(\theta, \phi)(\cos^2 \theta \sin^2 \phi + \cos^2 \phi) \quad (4.32)$$

and that which is parallel to the scattering plane is

$$I_{\parallel}(\theta, \phi, \chi) = \sigma I'(\theta, \phi) \left[\cos^2 \chi (\cos^2 \theta \cos^2 \phi + \sin^2 \phi) + \sin^2 \chi \sin^2 \theta \right]. \quad (4.33)$$

Equations (4.32) and (4.33) describe the perpendicular and parallel components of the scattered radiation along the ray to the observer. But these equations were derived for only a single ray from the nebula which is at a particular value of θ and ϕ . We therefore need to sum all of the contributions of rays from the nebula at every value of θ and ϕ . Since we do not have a functional form of $I'(\theta, \phi)$ but rather observed intensities at θ and ϕ , we can numerically solve equations (4.32) and (4.33) by the discrete sums

$$I_{\perp}(\chi) = \sigma \sum_{\theta} \sum_{\phi} I'(\theta, \phi)(\cos^2 \theta \sin^2 \phi + \cos^2 \phi) \quad (4.34)$$

$$I_{\parallel}(\chi) = \sigma \sum_{\theta} \sum_{\phi} I'(\theta, \phi) \left[\cos^2 \chi (\cos^2 \theta \cos^2 \phi + \sin^2 \phi) + \sin^2 \chi \sin^2 \theta \right]. \quad (4.35)$$

We have assumed spherical symmetry in our model. In determining $I'(\theta, \phi)$ we have made use of this symmetry by computing the mean intensity in a series of concentric annuli centered on the Rosette Nebula's expansion center which was determined by Kuchar and Bania (1993) to be $(l, b) = (206^{\circ}.266, -2^{\circ}.083)$ in galactic coordinates ($6^{\text{h}} 31^{\text{m}} 48.18^{\text{s}}, 4^{\circ} 58' 19.0''$ in equatorial coordinates). (This is within a few arc seconds of the central minimum which Celnik (1983) determined was $6^{\text{h}} 31^{\text{m}} 41.15^{\text{s}}, 4^{\circ} 58' 41.4''$ in right ascension and declination respectively.) Each annulus had a width of 1 pixel which corresponds to $1'.6$. A constant background was subtracted from each annulus.

The result is a radial plot of intensity across the Rosette Nebula which is shown in Figure 4.16. This plot, which is a function of the perpendicular distance from the center of the nebula, allows us to determine the intensity $I'(\theta)$ at the scattering point since we have assumed an spherical symmetry. Therefore, we

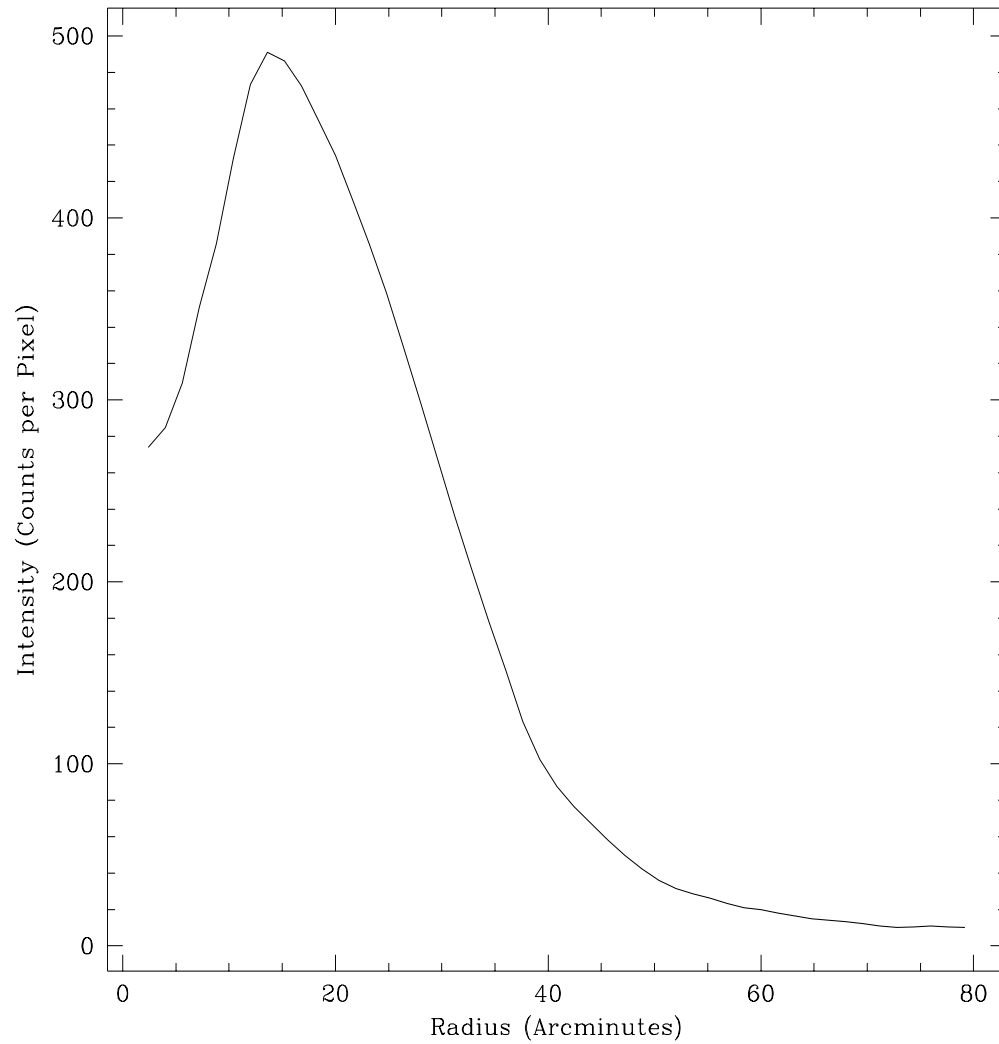


Figure 4.16 Radial plot of the flux of the Rosette Nebula. This plot was obtained by determining the mean flux in concentric rings about the center of the nebula. The width of each ring was $1'.6$.

can reflect this symmetry in equations (4.34) and (4.35) by integration about the angle ϕ instead of summing which yields the following equations

$$I_{\perp}(\chi, \theta) = \sigma \sum_{\theta} I'(\theta) (\cos^2 \theta + 1) \quad (4.36)$$

$$I_{\parallel}(\chi, \theta) = \sigma \sum_{\theta} I'(\theta) \left[\cos^2 \chi (\cos^2 \theta + 1) + 2 \sin^2 \chi \sin^2 \theta \right] \quad (4.37)$$

where we have used the fact that $\int_0^{2\pi} \cos^2 \phi d\phi = \int_0^{2\pi} \sin^2 \phi d\phi = \pi$.

Now with the aid of Figure 4.16 we can determine the perpendicular and parallel components of the scattered light for a single scattering particle at point P as shown in Figure 4.13. However, we need to consider the fact that the observed scattered radiation results from not one particle but rather many along the line of sight. That is to say, each particle in the vicinity of the Rosette Nebula that is along a particular line of sight will scatter radiation from the nebula into the line of sight and therefore equations (4.36) and (4.37) are modified by summing over the angle χ

$$I_{\perp}(\chi, \theta) = \sigma \sum_{\chi} \sum_{\theta} I'(\theta) (\cos^2 \theta + 1) \quad (4.38)$$

$$I_{\parallel}(\chi, \theta) = \sigma \sum_{\chi} \sum_{\theta} I'(\theta) \left[\cos^2 \chi (\cos^2 \theta + 1) + 2 \sin^2 \chi \sin^2 \theta \right]. \quad (4.39)$$

These equations are used to model the resulting polarization for particular distance from the Rosette Nebula. It was decided to base the model on the parameters of the HI cloud and extent of the HII region determined by Kuchar and Bania (1993) since these fit well with the observations of where polarization exist in our images. Consider the geometry shown in Figure 4.17 which represents a slice through the nebula and surrounding HI shell as seen from the top. The line of sight lies outside the HII region itself marked by radius r_n . We let the value of r_n equal $38'$ which is reasonable based on the fact that the nebular extent seen on the POSS red plate is about $38'$ and that the radio continuum emission mapped by Celnik (1985) in the direction of high polarization ends at

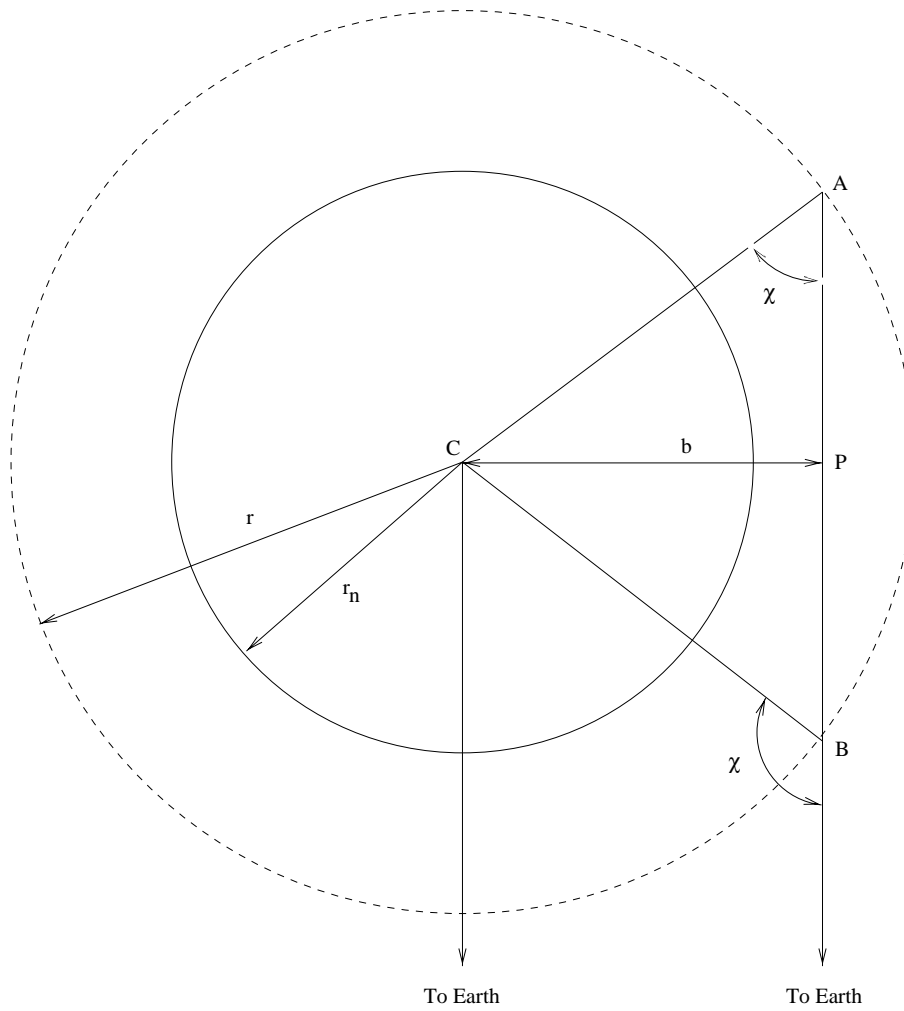


Figure 4.17 Geometry of the scattering model. The boundary of the HII regions is labeled r_n , the radius of the scattering cloud r_c . Integration is along the line of sight from A to B .

about $40'$. The outer radius marked by the dashed circle r_c in Figure 4.17 marks the farthest extent of a spherical cloud of scattering particles. We decided to let this radius extend to $60'$ which corresponds to about the maximum extent of the HI shell surrounding the nebula. Therefore, integration of I_{\perp} and I_{\parallel} are from the points labeled A to B through the cloud of scattering particles. From the geometry used, χ is the angle between the line segments CA and AP where C is the center of the nebula and P is the point along the line of sight and perpendicular distance from the center of the nebula as shown in Figure 5.0. (We denote this perpendicular distance by b and call it the impact parameter.) Since we are integrating along the line of sight, the angle χ will of course change from an acute to an obtuse angle. Therefore, we need a method to determine χ at various places along the line of sight.

Consider a point D along the line of sight between A and B as shown in Figure 4.18. We wish to determine the angle χ at this location so that it may be used in equation (4.39) to determine I_{\parallel} . Given the impact parameter b the distance \overline{AB} is

$$\overline{AB} = 2\sqrt{r_c^2 - b^2}. \quad (4.44)$$

We divide the line segment \overline{AB} into an equal number of steps N . Therefore, the length of each step is $\Delta = \overline{AB}/N$. After n number of steps from point A , the distance q from point B to point D is

$$q = \overline{AB} - n\Delta = (N - n)\Delta. \quad (4.45)$$

Now the triangle BCD has sides of length r_c , q , and h , where h is the distance from the center of the nebula to point D . The distance h is easily determined by the law of cosines, $h^2 = q^2 + r_c^2 - 2qr_c \cos(\beta)$ where β is the angle between the line segments \overline{BC} and \overline{BD} . This angle is a constant and can be easily determined from the values of b and r_c as $\beta = \sin^{-1}(b/r_c)$. Therefore, from the determination of β , h , and q the angle χ is found from the law of cosines to be

$$\chi = \cos^{-1} \left[\frac{h^2 - r_c^2 + q^2}{2hq} \right]. \quad (4.46)$$

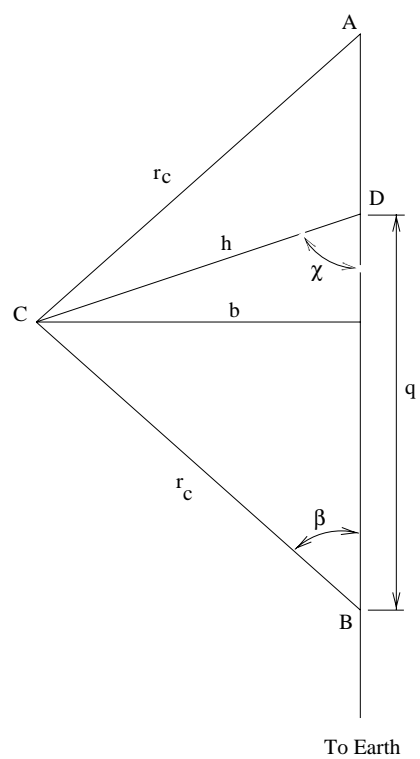


Figure 4.18 Figure used to help determine the angle χ at a point along the ray \overline{AB} through the scattering cloud.

From the discussion above we see that the only parameters needed for the model are the radius of the HII region r_n , the outer radius of the scattering cloud r_c , the impact parameter b , and the number of steps along the line of sight N through the scattering cloud. Reasonable choices of r_n and r_c were made from information already given by observations and these in turn dictate choices for the impact parameter. The number of steps is easily determined from the results of the calculation. Computing the percent polarization for various values of N will yield different results. However, for large value of $N > 100$, the value of percent polarization calculated does not significantly change. In fact, it was found that convergence occurred quickly. Therefore, the number of steps was chosen to be large enough so that the value of percent polarization varied by less than 1%. It should also be pointed out that percent polarization calculated for a single angle χ did not change significantly when the number of steps through θ was greater than 1000. Therefore, the number of steps through θ was always 1000 and the number of steps N along the line of sight was typically 1000 as well.

We show in Figure 4.19 and 4.20 the result of percent polarization and intensity predicted as a function of impact parameter using the value of r_c, r_n , and N discussed above. From the two figures we see that polarization has a very high initial value and continues to rise, whereas the intensity drops. The drop in intensity is expected because the geometry of the situation requires a shorter path length through the nebula as the distance from the nebula increases and flux from the nebula before scattering drops $\sim 1/r^2$, (i.e. the nebula subtends a smaller solid angle). As seen in Figure 4.19, the predicted percent polarization is much higher than is observed. Whereas the model predicts a continual increase over increasing radial distance from the nebula, the actual behavior is an increase in polarization followed by a decline after reaching a maximum value. The intensity predicted by the model was determined by summing the two orthogonal components of polarization predicted by equations (4.38) and (4.39). This intensity can not be strictly evaluated because the multiplying factor of the particle's scattering cross-section and particle density is unknown.

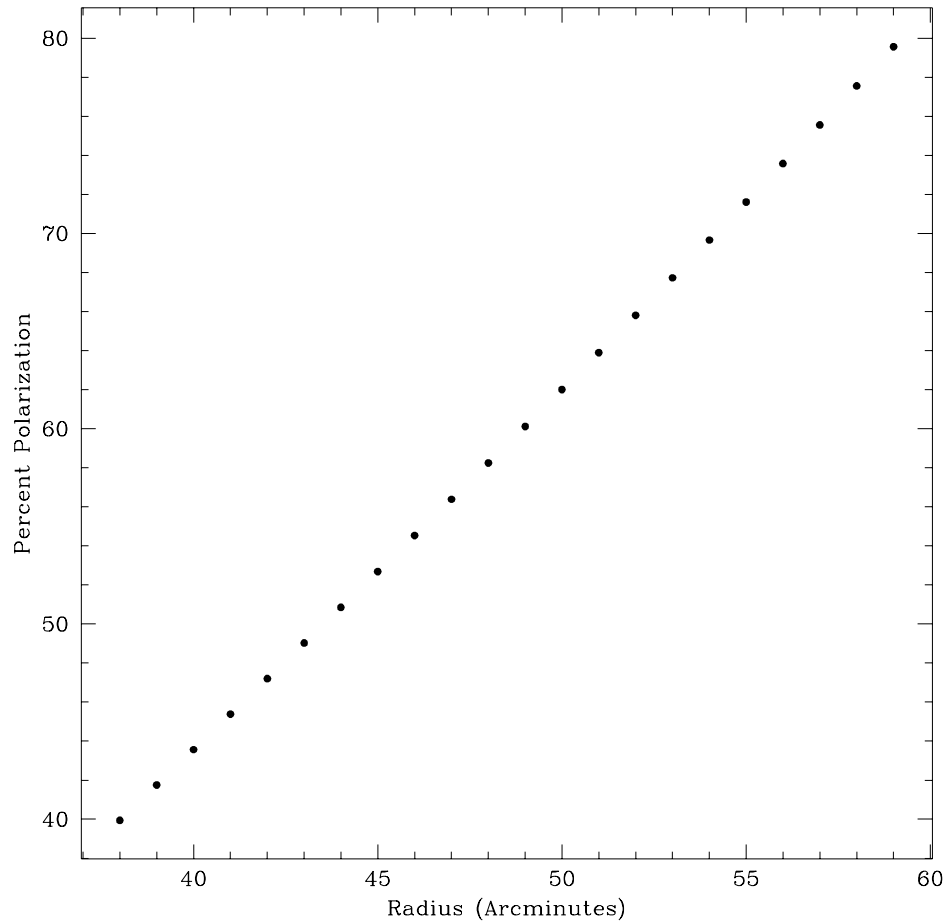


Figure 4.19 Results from the modeled polarization. The impact parameter is the location of the scattering beam from the HII region through the cloud of scattering particles.

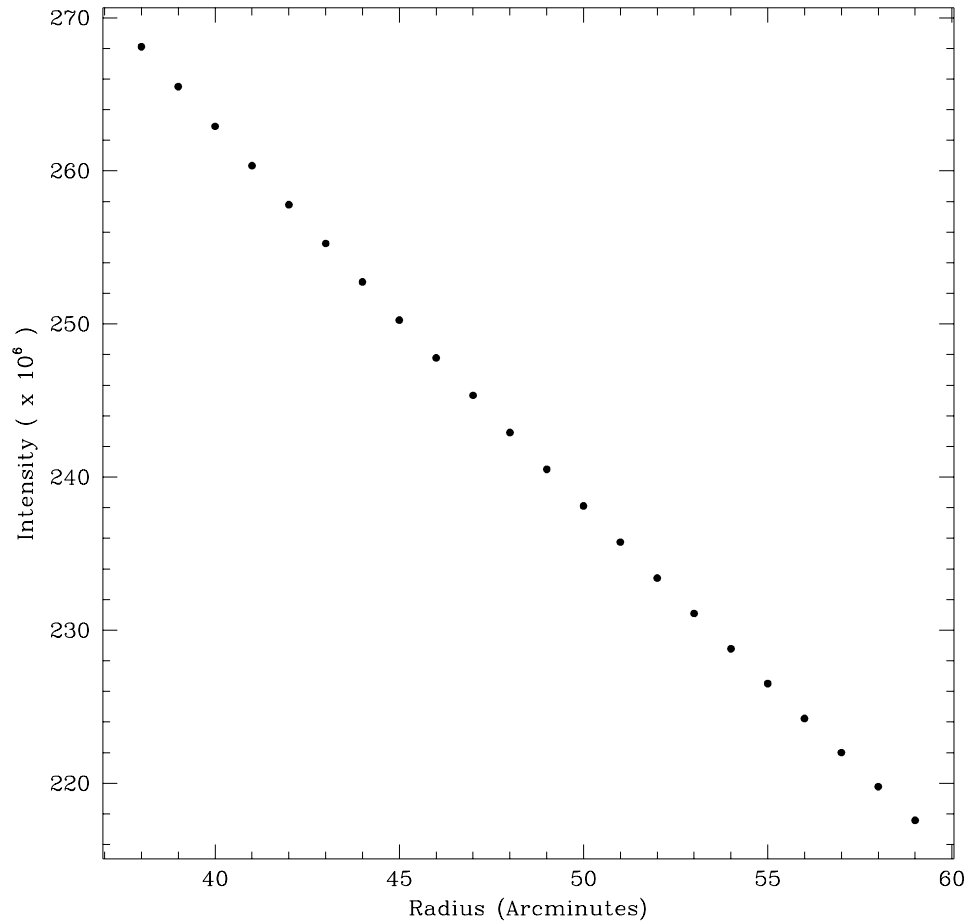


Figure 4.20 Predicted intensity as a function of radial distance from the HII region through the scattering cloud. The value of intensity can not be strictly interpreted since the cross-section of the scattering particle is unknown.

The model was tested by calculating the value of polarization expected at particular incident scattering angles χ with θ set to zero. The expected behavior is an increase in polarization as χ increases, reaching a maximum at 90° , and then declining again, all the while maintaining symmetry around the maximum at 90° . This is observed when values of polarization are calculated in special cases using equations (4.38) and (4.39) as well as from the computer program. Therefore, I am confident the program is correct.

I also point out that our model yields values of polarization similar to another single scattering model of similar geometry by Jura (1978). His predictions of the degree of polarization for emission from a homogenous sphere yields values on the order of 20 to 80 percent for a scattering particle very close to the source of emission. Both models, therefore, are not able to predict the expected degree of polarization.

I conclude that my model is inadequate at predicting the behavior of polarization based upon a single scattering hypothesis. A multiple scattering model, however, would change the story. Since the region traversed by a ray through the cloud can be rather large, the scattering of light into and out of the ray is most likely an important consideration. The process of multiple scattering would have the effect of reducing the degree of polarization observed since the intensity of light reaching the ray comes from not only the nebula but also scattered light from the surrounding dust cloud. This has the overall effect of making the light appear more isotropic at the location of scattering, hence reducing the polarization. Therefore, the problem should be more realistically tackled by a multiple scattering model. However, such a model is beyond the scope of this dissertation since it, in and of itself, would be a dissertation. A search though the astronomical literature has revealed numerous models on multiple scattering, none of which are applicable to the geometry at hand.

4.5.3 The Correlation of $H\alpha$ with Infrared

In order to provide further evidence for the case of polarization by scattering, we compared the $H\alpha$ intensity observed in the region of suspected scattering with infrared emission using images taken by IRAS, the Infrared Astronomical Satellite. Since we believe dust particles are the scattering agent responsible for the $H\alpha$ emission seen in the region of high polarization, we expect a correlation to exist between $H\alpha$ and infrared emission since the latter arises from heated dust grains.

The Rosette Nebula shows up in all four wavebands ($12\mu\text{m}$, $25\mu\text{m}$, $60\mu\text{m}$, and $100\mu\text{m}$) of the IRAS images. Cox et al. (1990) have analyzed the Rosette Nebula using the IRAS data. From their analysis, Cox et al. found that the $60\mu\text{m}$ and $100\mu\text{m}$ emission originates in both the ionized gas of the HII region as well as in the surrounding neutral gas. The bulk of the $25\mu\text{m}$ emission was shown to be confined to the HII region itself. However, comparing the IRAS data with the radio continuum data of the Rosette from Celnik (1985), they find the $12\mu\text{m}$ emission to be coming from a region behind the ionization front outside the HII region. They show that the $12\mu\text{m}$ emission comes from a shell surrounding the ionized gas. Since the $60\mu\text{m}$ and $100\mu\text{m}$ emission is seen throughout both the HI and HII regions, and the $12\mu\text{m}$ emission is only seen in a shell outside the HII region, Cox et al. conclude that the grains emitting the $60\mu\text{m}$ and $100\mu\text{m}$ emission are fundamentally different from those responsible for the $12\mu\text{m}$ emission. Whereas the emission from $60\mu\text{m}$ and $100\mu\text{m}$ is taken to be those of large silicate grains with ice mantels in HII regions, the $12\mu\text{m}$ emission is believed to originate from very small grains probably in the form of aromatic hydrocarbons. Similarly, the grains responsible for the $25\mu\text{m}$ emission are probably different than the PAHs (Polycyclic Aromatic Hydrocarbons) thought to be responsible for the $12\mu\text{m}$ emission.

Since evidence points to the existence of small grains in a shell outside the HII region, we looked to see if there was any correlation between this emission and the $H\alpha$ intensity we observed at the location of high polarization which is beyond the boundary of the HII emission. A comparison was first made between the intensity of $H\alpha$ and infrared at all four wavelengths. We suspect that since infrared emission at all four wavelengths is seen in this region, there should exist a correlation between emission in all four wavebands and $H\alpha$. We then looked

at the relationship between percent polarization observed and the $12\ \mu\text{m}$ emission in the region.

Since our goal was to see if a correlation existed by comparing the $\text{H}\alpha$ and infrared intensities, no major data reduction steps were performed on the IRAS images; only the determination of a background for subtraction and smoothing by median filter. The IRAS images were obtained from the *SkyView** astronomical survey database on the world wide web. To make comparing the IRAS and $\text{H}\alpha$ images easier, the image centers and orientations were chosen to match those from SLIC. Since the pixel scale of the IRAS images closely matches our own, scaling was not performed. Since the $\text{H}\alpha$ images were smoothed using a 3×3 median filter, each of the four IRAS images were smoothed in exactly the same manner as the $\text{H}\alpha$ images. A background was determined by calculating the mean in a small 3×3 box at various places around the image where emission was low, or at least, not obvious. An average background from these values was calculated and subtracted from each pixel in the image.

The first comparison made was between $\text{H}\alpha$ and the IRAS emission in all four wavebands at the region of high polarization shown in Figure 4.8. A plot of IRAS versus $\text{H}\alpha$ intensity was made and the results are presented in Figure 4.21. As the figure shows, a positive correlation appears to exist between $\text{H}\alpha$ and infrared in all four wavebands. To quantitatively assess the correlation, the Pearson ρ was computed for each of the four graphs and was found to be approximately ~ 0.85 which has a 95% confidence interval $\sim [0.82, 0.87]$. The confidence interval computed merely states that we are 95% certain that ρ is between these two values. The Pearson ρ is not very good at determining whether this observed correlation is statistically significant since it has no knowledge of the underlying distributions. A look at the graph does however indicate, at least visually, that a correlation between $\text{H}\alpha$ emission and infrared emission at all four wavebands.

**SkyView* was developed under a NASA grant with principle investigator Thomas A. McGlynn under the auspices of the High Energy Astrophysics Archive Research Center (HEASARC) at the GSFC Laboratory for High Energy Physics.

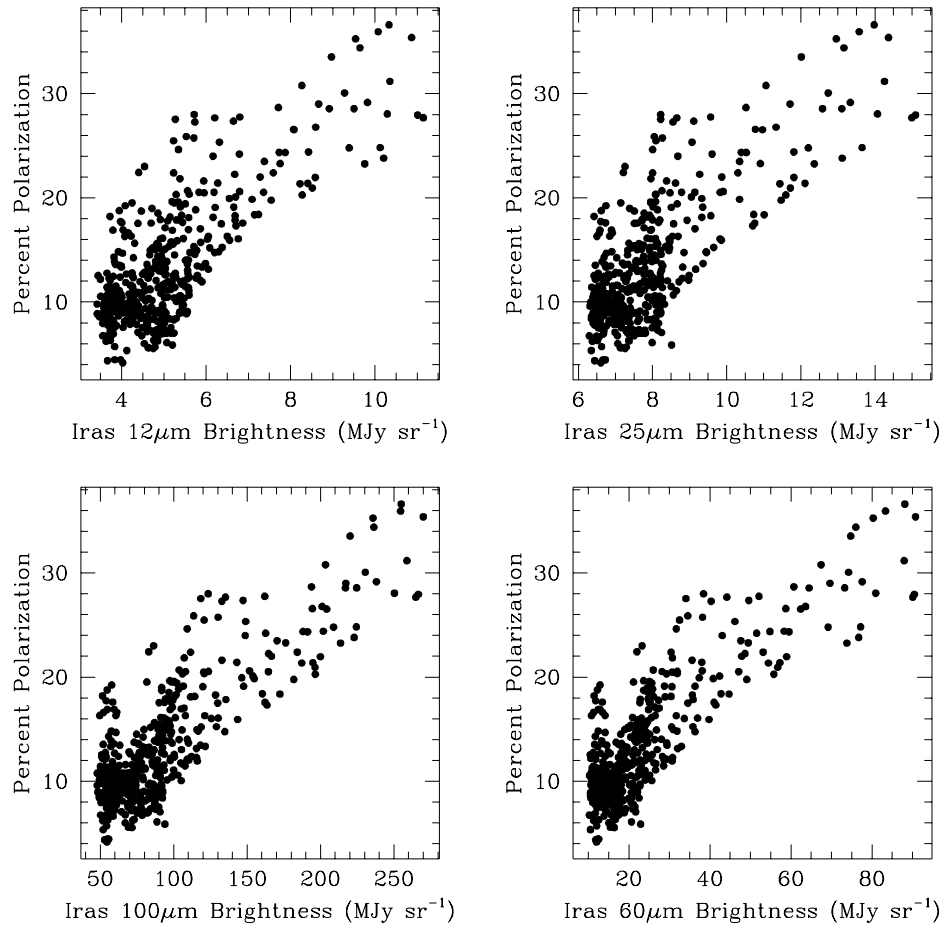


Figure 4.21 $H\alpha$ brightness versus infrared emission at $12\mu\text{m}$, $25\mu\text{m}$, $60\mu\text{m}$, and $100\mu\text{m}$. These IRAS infrared images were obtained from the *SkyView* astronomical sky survey database on the world wide web.

In order to show the relationships in Figure 4.21 in a different way, radial plots of $H\alpha$ versus emission in all four wavebands were created. These are shown in Figure 4.22. Here the data is reduced to one dimension, but unlike Figure 4.21, there is less scatter in the data because of binning. The x and y position values were converted into radii from the center of the nebula and placed in bin width of 2 pixel radius ($3.2''$). The average was computed for both the infrared and $H\alpha$ intensities in each bin, as well as the standard deviation of these averages. Figure 4.22 is the resulting graph with standard deviation of the mean as error bars. For each of the graphs, correlation appears to exist between the $H\alpha$ and infrared emission in all four wavebands. I suggest that the positive correlation is evidence that scattering of $H\alpha$ emission from the Rosette Nebula is linked to emission in the infrared.

As a second test to see if emission by dust in the infrared is correlated with the $H\alpha$ scattering observed, I looked at the comparison of IRAS emission at $12\ \mu\text{m}$ and the percent polarization. For each pixel where polarization is seen in the region of high polarization, we compared this value of percent polarization with the corresponding $12\ \mu\text{m}$ emission. The result is seen in Figure 4.23. We see a unique behavior, unlike that in the comparison of intensities. In Figure 4.23 the polarization is initially seen to rise with increasing $12\ \mu\text{m}$ emission, but peaks and then declines. Bright values of $12\ \mu\text{m}$ emission are from regions near the border of the HII region. The polarization peaks between $40'' - 50''$ in radii and then starts to decline. As can be seen in Figure 4.23, there is a lot of scatter in the data, however, the overall polarization decreases as the line of sight moves further out from the nebula. This overall decrease in polarization can be explained qualitatively on the grounds of multiple scattering.

The increase in polarization is expected since the illumination becomes increasingly anisotropic as you move further from the border of the HII region. At the border of the Rosette Nebula, the HII region subtends a solid angle of 2π steradians. At this location, the source of illumination appears more isotropic than if it were farther away. As the line of sight moves away from the Rosette Nebula, the HII region subtends a smaller angle, increasing the anisotropy of the radiation field, thus increasing the polarization by scattering. As you move far away, however, the radiation starts to become more isotropic again due to multiple scattering, driving down the polarization.

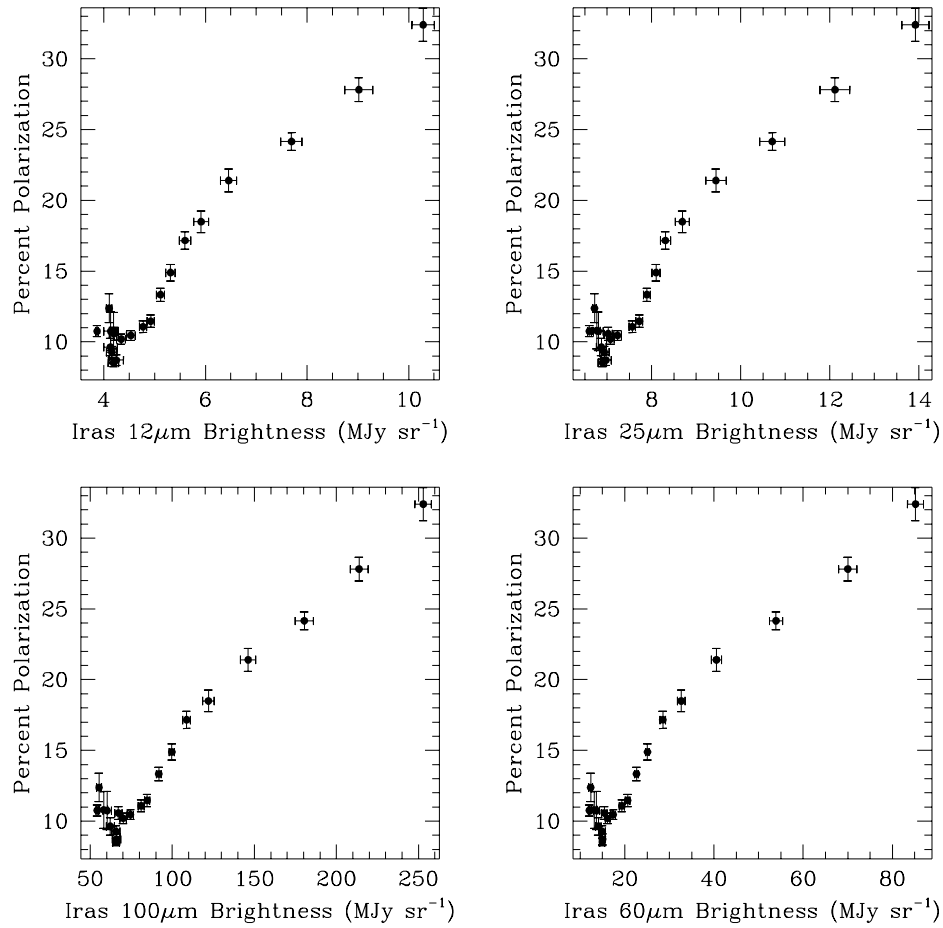


Figure 4.22 Radial plots of H α versus four different wavebands of infrared emission. These are radial averages in bins 3'.2 in width from the center of the nebula corresponding to the graphs in Figure 4.21.

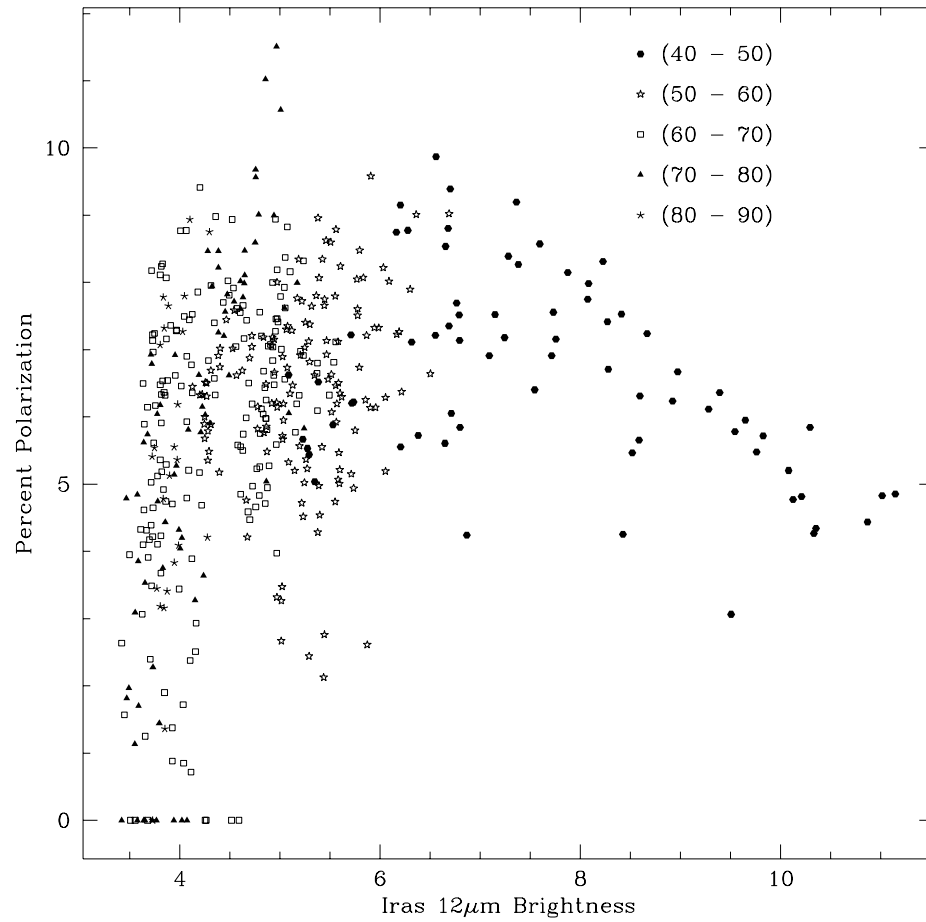


Figure 4.23 Comparison between the percent polarization and IRAS 12 μm brightness in the region of high polarization shown in Figure 4.8.

We believe we are seeing this effect in the behavior of the percent polarization versus the $12\ \mu\text{m}$ infrared emission. This, taken together with the correlation between the $\text{H}\alpha$ and infrared intensities in the region of high polarization, is, we believe, evidence for multiple scattering by dust grains in that region.

4.5.4 The Correlation of $\text{H}\alpha$ with [SII]

Like the correlation of $\text{H}\alpha$ with infrared emission from the region of high polarization, another piece of evidence that points toward scattering is the correlation of $\text{H}\alpha$ intensity with [SII] intensity. While $\text{H}\alpha$ emission is formed by recombination by an electron after photoionization, [SII] is collisionally excited. Therefore, $\text{H}\alpha$ emission is a measure of the number of photons present in the gas while [SII] emission is sensitive to the number of electrons present. A comparison of $\text{H}\alpha$ with [SII] reveals information about the excitation conditions. Inside HII regions, radiative excitation is enhanced relative to collisional excitation. This implies that the expected ratio of [SII]/ $\text{H}\alpha$ would be reduced. Observations by Reynolds (1985,1988) have revealed this to be the case for HII regions. Regions where collisionally excitation is enhanced relative to radiative excitation, such as in shocks, would have a higher value of the [SII]/ $\text{H}\alpha$ ratio. Therefore, measuring the [SII] to $\text{H}\alpha$ ratio as a function of radial distance from the nebula center outward, we expect this ratio to yield information about the excitation conditions in and around the nebula.

A series of $\text{H}\alpha$ and [SII] images were taken on the nights of 17 October 1998 and 10 February 1999. On the first night above, images of NGC 7000 (the North America Nebula) and NGC 1499 (the California Nebula) were obtained as part of a [SII] survey in progress by Dr. Brian K. Dennison and Dr. John H. Simonetti. Similarly, on the second night, a series of five consecutive images of NGC 1499 and the Rosette Nebula were obtained in both $\text{H}\alpha$ and [SII].

The process used to create the [SII]/ $\text{H}\alpha$ ratio images were slightly different than the ones used to create the polarization maps. The nominal reduction steps were the same. These included correcting the images by removing a bias and flat-fielding as well as transposing the images. They were also in need of alignment. Since images of the of the NGC 1499 were interspersed among other images taken that night, they were shifted by a large number of pixels. In order

to achieve accurate alignment, the transformation process was performed using the **GEOMAP** and **GEOTRAN** task in **IRAF**. These are similar to the **IMALIGN** task used to align the polarization images. In this process, a series of bright stars visible in both images were used as reference points for alignment. A reference image was chosen and accurate centers for the reference stars were calculated using the **CENTER** task. Similarly, accurate centers for those very same stars in the images needing shifting were computed. A single file relating the two sets of stellar positions was created as the input file for **GEOMAP** which computes the amount of shifting and rotation necessary to bring the set of stellar points into alignment with the reference stars in the reference image. The output of **GEOMAP** is then used along with the stellar list as input files for **GEOTRAN** which does the actual shifting of the images. As with the polarization images, the bicubic spline was chosen since it has been shown previously to be the algorithm which least alters the image of extended sources.

Once all the images were aligned, the removal of a background was necessary. Before this was done however, the images were median filtered to remove faint stars and to increase the overall signal-to-noise ratio. The task **MEDIAN** was used, and the median inside a 3×3 box centered on every pixel in the image was computed. The pixel value was then replaced by the computed median value. This was done for every pixel in the image, with the border of the image being disregarded since it is an unused area. A background was then determined for these smoothed image by calculating the statistics inside a 3×3 box at various places where the $H\alpha$ or **[SII]** brightness was at a minimum. A series of places were chosen for each image and the median background at these locations were averaged to obtain an overall value of the background. This value was then subtracted from each pixel in the image using the **IMARITH** task. An average background for each image was subtracted.

At this point, the **[SII]** images were divided by their corresponding $H\alpha$ image. Since all images were three minute exposures, there was no need to scale them to a common integration time. Data taken on the night of 17 October 1998 resulted in four **[SII]/ $H\alpha$** ratio images of the California Nebula and six ratio images of the North America Nebula. These images were then averaged using the **IMCOMBINE** task with the maximum value rejected before averaging at every pixel site. For the images taken on the night of 10 February 1999, there were three **[SII]/ $H\alpha$** ratio images of the California Nebula as well as five ratio images of the Rosette Nebula. Again, these were combined to create a final

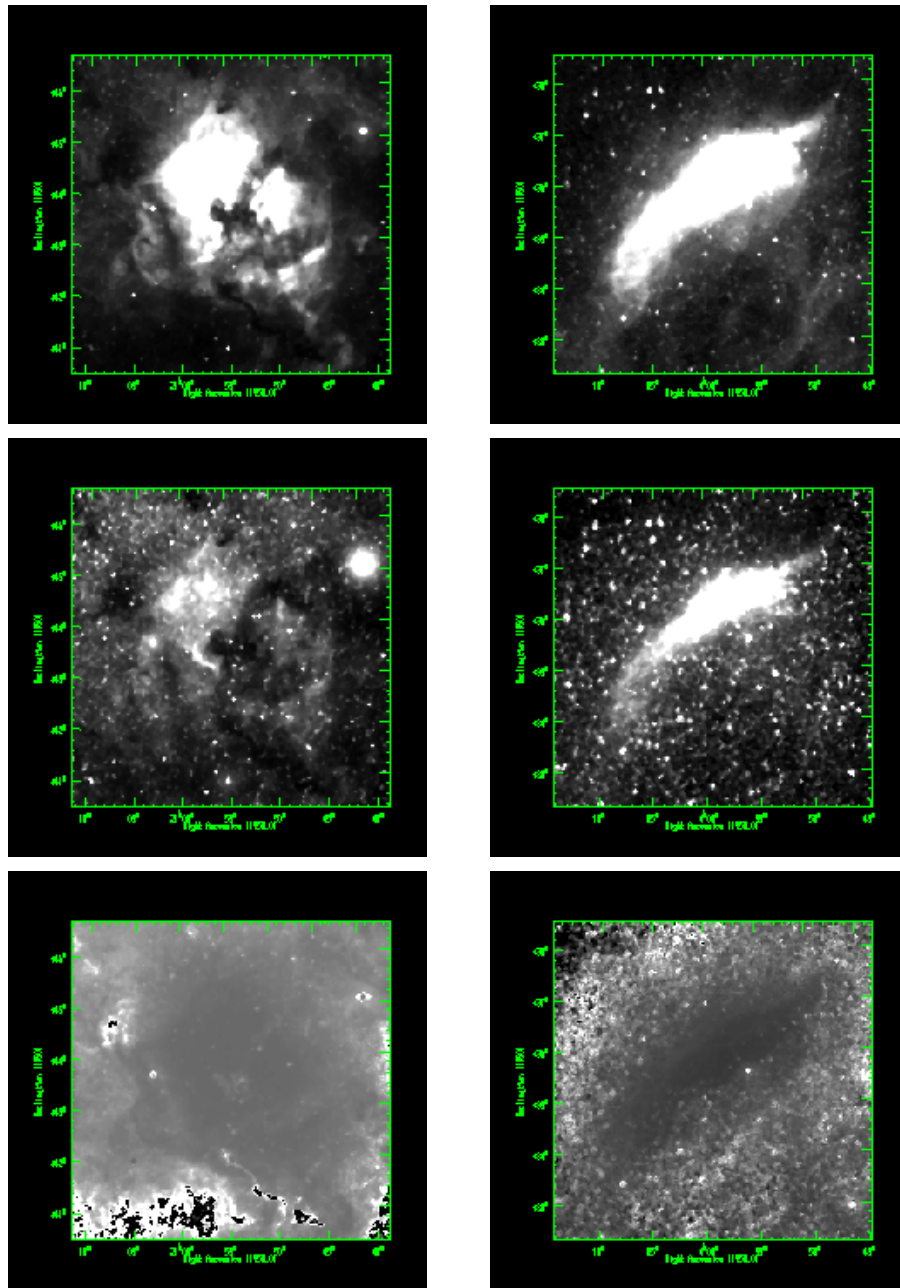


Figure 4.24 $H\alpha$, [SII], and [SII]/ $H\alpha$ images (*from top to bottom*) of NGC 7000 (*right*) and NGC 1499 (*left*).

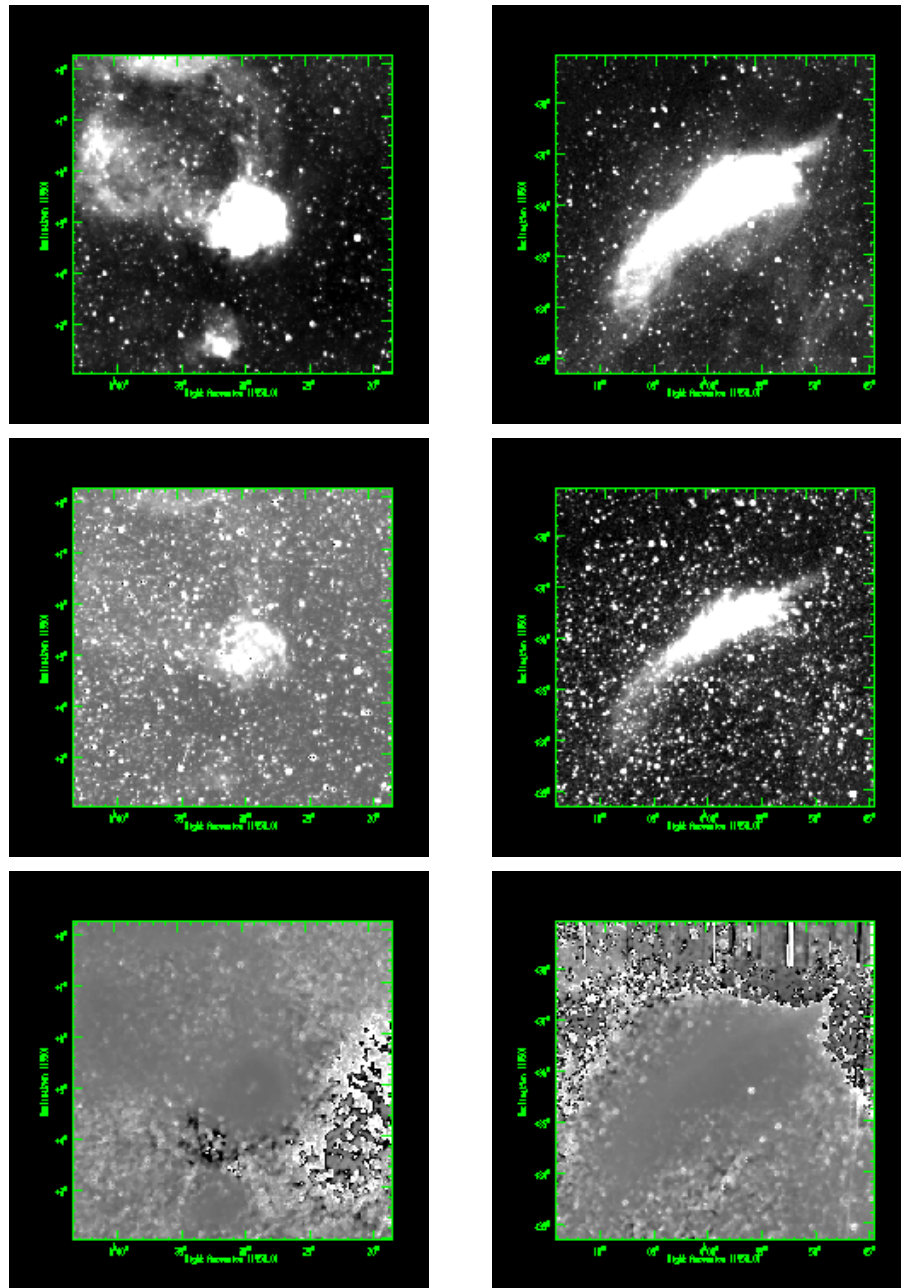


Figure 4.25 H α , [SII], and [SII]/H α images (*from top to bottom*) of the Rosette Nebula (*right*) and NGC 1499 (*left*).

averaged ratio image. The $H\alpha$, [SII], and [SII]/ $H\alpha$ ratio images are shown in Figure 4.24 and 4.25. Only the areas of interest, the North America, California, and Rosette Nebulae are shown. (That is, these are sub images of larger images.)

As a check of consistency and to look for any night-to-night variations in the [SII]/ $H\alpha$ ratio, a comparison was made between the two images of NGC 1499 taken on two different nights. We also checked to see if the [SII]/ $H\alpha$ ratio values of NGC 7000 were in agreement with published results from Reynolds (1985,1988). We found that inside NGC 7000, the ratio of [SII]/ $H\alpha$ is typically on the order of 0.1 – 0.2 at its lowest and becomes increasingly higher farther away from these regions. We found similar results for NGC 1499. As a check for night-to-night variations, a comparison was made between the two NGC 1499 images obtained on different nights. The mean ratio inside a 3×3 box was obtained, along with the standard deviation inside the box, at five different places inside the nebula. These measurements were made at identical locations in each image of the California Nebula so that an accurate comparison could be made. The results are listed in Table 4.2 below. It can be seen from the data that, except for the first location, measurements of the ratios are consistent from night-to-night.

Table 4.2
MEAN RATIO OF [SII]/ $H\alpha$ IN NGC 1499

Position	(First Night)		(Second Night)	
	Mean	σ	Mean	σ
$3^{\text{h}} 54^{\text{m}} 52^{\text{s}}.7, 35^{\circ} 52' 49''.5$	0.16	0.02	0.29	0.02
$4^{\text{h}} 02^{\text{m}} 37^{\text{s}}.7, 35^{\circ} 45' 50''.6$	0.37	0.02	0.36	0.02
$3^{\text{h}} 58^{\text{m}} 49^{\text{s}}.5, 36^{\circ} 07' 37''.8$	0.24	0.01	0.26	0.01
$3^{\text{h}} 55^{\text{m}} 39^{\text{s}}.2, 36^{\circ} 27' 07''.1$	0.32	0.04	0.29	0.03
$4^{\text{h}} 01^{\text{m}} 06^{\text{s}}.3, 26^{\circ} 28' 55''.5$	0.18	0.01	0.21	0.01

Having checked the values for consistency, we then made measurements of the ratio of [SII]/ $H\alpha$ for the Rosette Nebula, particularly in the region of suspected scattering. Since we believe the light seen in this area results from scattering by interstellar dust grains, the light seen in this region should have the similar characteristics as that which last left the nebula. That is to say, if this light is truly scattered $H\alpha$ emission from the Rosette Nebula, then we expect it to have a similar ratio of [SII]/ $H\alpha$ as the light which last left the emission

region. Since [SII] and $H\alpha$ lines are very close in wavelength, we expect scattering to be almost the same for both.

In order to make this determination, the [SII]/ $H\alpha$ ratio in a wedge of points from the center of the nebula to the scattering region were measured. (Figure 4.26 shows the location of all the points in the wedge.) Each x and y location in the wedge was then converted into a radial distance from the center of the nebula, and the values binned to create a radial plot. The bin width was $3'.2$ and all [SII]/ $H\alpha$ ratio values in that bin were averaged. Using the radial plot of the wedge shown in Figure 4.27, we see how the ratio of [SII]/ $H\alpha$ changes radially from the center of the nebula out to the suspected scattering region. The radial graph has several features which are explained as follows.

First, there is a decrease in the [SII]/ $H\alpha$ ratio as you move outward from the center of the Rosette Nebula, reaching a minimum at around $\sim 15'$. This is easily explained by the fact that no stars were removed from the image and what we are seeing is the result of contamination by starlight in the central cavity of the Rosette Nebula. The minimum at around $15'$ is also approximately the radius of the star cluster NGC 2244. From $\sim 15'$ on, the ratio of [SII]/ $H\alpha$ increases until $35'$ where it peaks and starts to slightly drop again. The increase is expected since farther from the source of excitation (star cluster) there are fewer ionizing photons, which implies that collisional excitation becomes somewhat more important relative to radiative excitation. The peak at $35'$ roughly corresponds to the radius at where the curved polarization vectors start, but not where the continuum emission observed at 4850 MHz by Celnik (1985) cuts off (as seen in Figure 4.28). The radio continuum emission ends at just a little more than $40'$ in the wedge region. While the radial plot of [SII]/ $H\alpha$ does show variation between $35' - 60'$, there is no large increase in the ratio between these two radii. While there does appear a slight increase in the ratio of [SII]/ $H\alpha$, it none-the-less remains relatively flat from $35' - 60'$. Figure 4.28 shows that at around $50' - 60'$ we have reached the southern boundary of the nebula marked by the 3σ contour.

The effects of bright stars on the radial profile of [SII]/ $H\alpha$ are seen in Figure 4.23 at its two extremes. I questioned what effect the removal of these stars would have on the radial profile plot. Using the task DAOFIND in IRAF we were able to quickly and accurately locate a large number of bright stars in the image. The detection limit was set to find point source that were 15σ above

background. Two of the stars that were found were the ones at the location of the "horn" discussed above. A few more were at the center of the nebula, as well as in the region delineated by the wedge. A 2×2 box of pixels at these stellar locations were removed and the same process of making the radial plot was done. This new radial plot is shown in Figure 4.29. In it we see that the curve no longer has a positive value of 0.2 at the center of the nebula, but rather < 0.1 . With increasing radial distance, the curve is seen to rise, again reaching a peak value at around $35'$ before going slightly down. This same general behavior is seen in this graph as was before the stars were removed. There is also a tendency to flatten out between $35' - 60'$ with only a slight, overall increase. The variation has also becomes slightly less than before and the error bars on the points at greatest radial extent have increased. This is to be expected since the removal of points decreases the square root in the denominator of the standard deviation of the mean. The new radial plot only enhances the evidence for scattering.

Therefore, from the behavior of the radial profile of $[\text{SII}]/\text{H}\alpha$ in the wedge region we conclude that this is further evidence that the $\text{H}\alpha$ intensity in this particular region of the Rosette Nebula is scattered $\text{H}\alpha$ emission from the nebula. Its relatively flat nature in the region, and the fact that the $[\text{SII}]/\text{H}\alpha$ ratio in this region is roughly equal to the value that last left nebula lead us to believe that the light in the region of high polarization is in fact scattered $\text{H}\alpha$ emission which last left the Rosette Nebula.

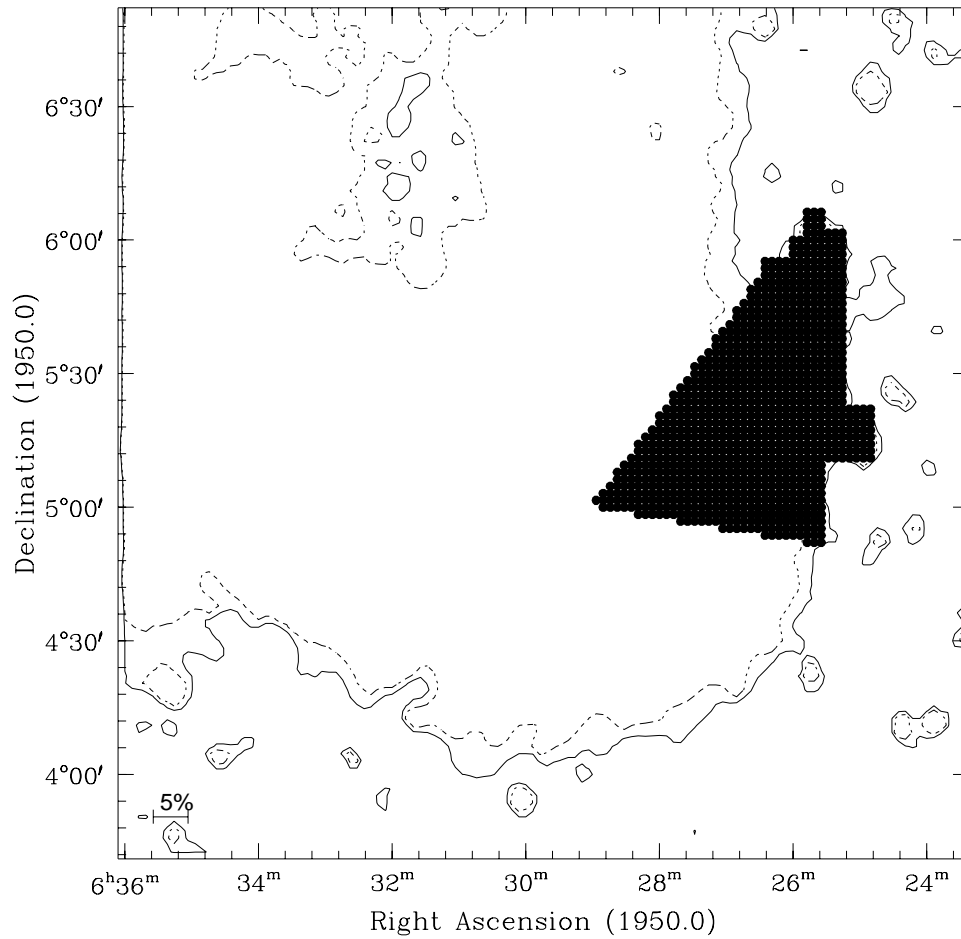


Figure 4.26 Contour plot of the Rosette Nebula showing the location of points in a wedge pattern where measurements of the $[\text{SII}]/\text{H}\alpha$ ratio were made. Contours are 3σ (solid) and 5σ (dashed) above background.

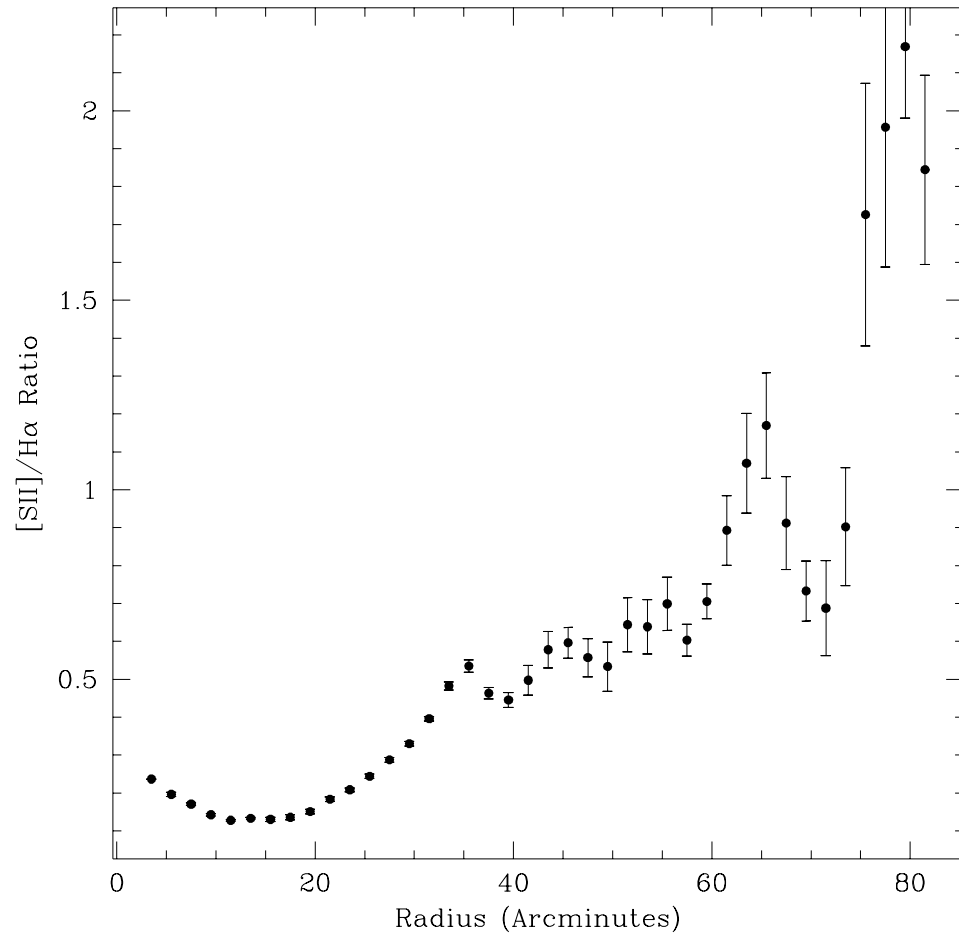


Figure 4.27 Radial profile plot of points inside the wedge region of the Rosette Nebula seen in Figure 4.26.

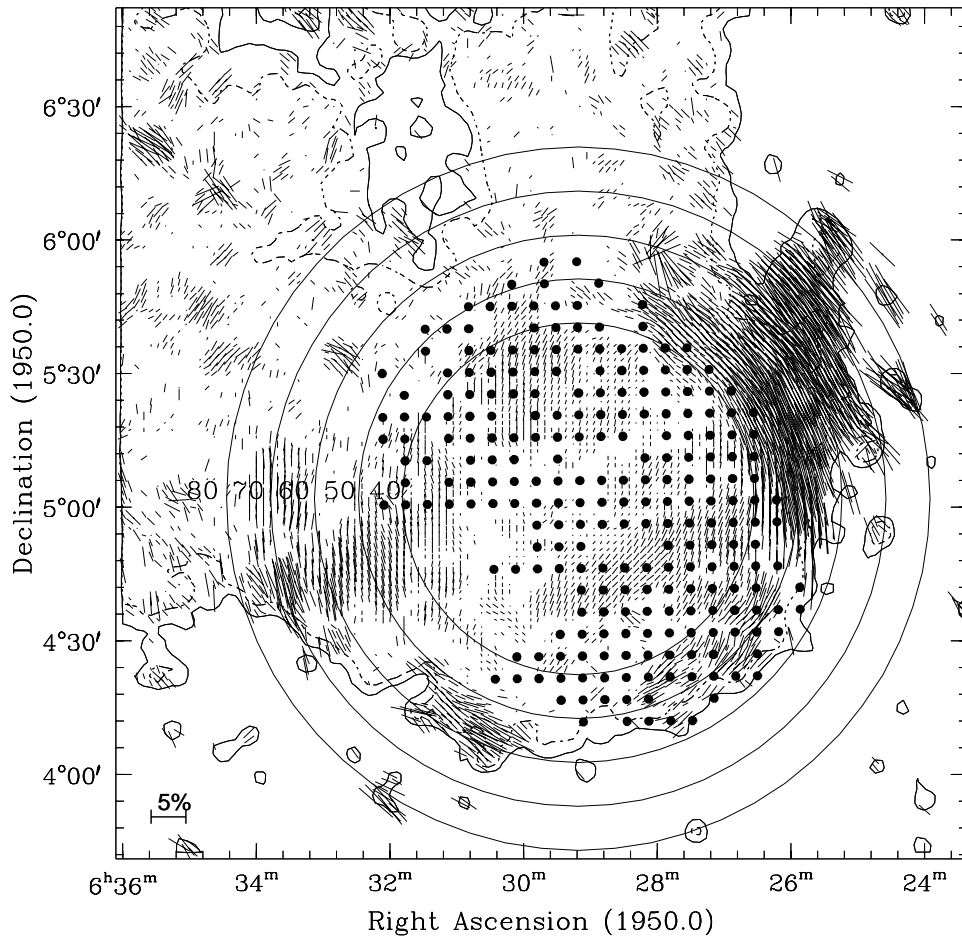


Figure 4.28 Contour plot of the Rosette Nebula with polarization vectors. The heavy dots indicate areas where radio continuum emission values were taken from the 4850 MHz continuum image by Celnik (1985). Concentric radii circles are measured in arcminutes and are centered on the H α minimum.

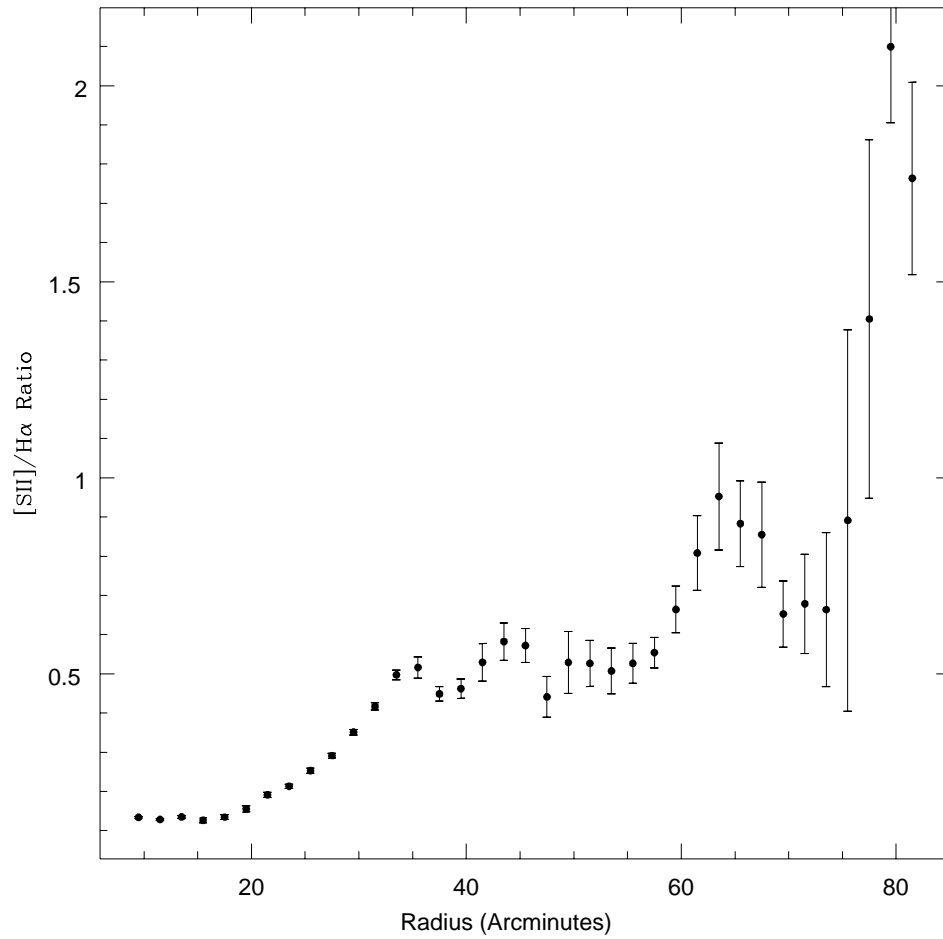


Figure 4.29 Radial profile plot of [SII]/H α for the wedge region of the Rosette Nebula shown in Figure 4.27 but with stars removed from the wedge region.